On the sensitivity of elastic waves due to structural damages: Time–frequency based indexing method

R. Gangadharan, D. Roy Mahapatra*, S. Gopalakrishnan,
C.R.L. Murthy, M.R. Bhat

Department of Aerospace Engineering, Indian Institute of Science, Bangalore 560012, India

Abstract

Time–frequency analysis of various simulated and experimental signals due to elastic wave scattering from damage are performed using wavelet transform (WT) and Hilbert–Huang transform (HHT) and their performances are compared in context of quantifying the damages. Spectral finite element method is employed for numerical simulation of wave scattering. An analytical study is carried out to study the effects of higher-order damage parameters on the reflected wave from a damage. Based on this study, error bounds are computed for the signals in the spectral and also on the time–frequency domains. It is shown how such an error bound can provide an estimate of error in the modelling of wave propagation in structure with damage. Measures of damage based on WT and HHT is derived to quantify the damage information hidden in the signal. The aim of this study is to obtain detailed insights into the problem of (1) identifying localised damages (2) dispersion of multifrequency non-stationary signals after they interact with various types of damage and (3) quantifying the damages. Sensitivity analysis of the signal due to scattered wave based on time–frequency representation helps to correlate the variation of damage index measures with respect to the damage parameters like damage size and material degradation factors.
© 2008 Elsevier Ltd. All rights reserved.

1. Introduction

Not much research has been reported on the parametric identification of various types of damages in structures using stress waves compared to the research done using vibration and modal analysis and test data. The existence of damage in a structure is generally traced by comparing the time-domain travelling wave response of the structure at its present state with a base-line response. Any fluctuation from the base-line response is correlated to the damage location through the time of arrival of the new peaks (scattered waves). This is also true for damage initiation and progression in the form of strain energy release from the damaged zone that arrives at the measurement location in the form of transients. Therefore by employing the wave based methods, the presence of damage in a structure is detected by looking at the wave parameters affected

---

*Corresponding author: Tel.: +91 80 3942757; fax: +91 80 3600134.
E-mail addresses: droymahapatra@aero.iisc.ernet.in, droymahapatra@yahoo.co.in (D.R. Mahapatra).

by the damage. The wave parameters that are commonly used for damage detection are the parameters representing attenuation and reflection of waves due to damage, mode conversion, etc. Numerical simulation based on a parameterised model becomes useful for this purpose.

For localised and small size of damages such as matrix cracks, delaminations and fiber fracture in composite, a Lamb wave-based interrogation technique is most suitable for identification and quantification of damage. In composites, the percentage of degradation of ply properties can be considered as a set of parameters. Similar parametric representation or idealisations are also possible for other types of damages, such as transverse micro-cracks in cross-ply laminates, progressive damages leading to delamination and fiber fracture, etc.

In order to overcome various computational problems like large system size, mesh sensitivity, numerical stability and accuracy in the *hp*-finite element model for wave scattering, a spectral finite element method (SFEM) has been developed [1]. The SFEM formulation for wave propagation in composite beams using Euler–Bernoulli beam theory and first-order shear deformation theory (FSDT) was reported by Mahapatra et al. [2,3]. To model the damages like transverse matrix cracking in a composite beam, the degraded material properties are substituted in the damaged portion of the beam. With this type of mechanistic description, a spectral element with degraded material properties was formulated by Garg et al. [4]. Spectral element with delamination type of damage in a composite beam was proposed by Nag et al. [5], where the exact dynamics of internally debonded sub-laminates was taken into account. This formulation then condense out the FE nodal information of the internal sub-elements, and hence allows one to replace an undamaged composite beam segment with a spectral element with damage where delamination may exists. Similar work was carried out by Ostachowicz et al. [6] to model delaminated composite beam using SFEM. Krawczuk et al. [7] have proposed the formulation of a finite composite beam element with an open crack. The damaged part of the beam has been modelled by a SFEM with a crack, while the undamaged part has been substituted by 3-node beam element. Ostachowicz et al. [8] have used SFEM to model wave propagation in damaged structures. The kinematics of a number of spectral finite elements to model damage, namely a cracked rod, a cracked Timoshenko beam, a delaminated multilayer composite beam, and cracked plate spectral finite elements was discussed. It is easily seen that spectral approach gives more information and is sufficient for damage detection. In the present work, SFEM is employed to simulate wave propagation in composites with various types of damages.

A major aspect of the problem under consideration is the identification of the reflection, mode conversion and scattering of the Lamb waves due to damage. It should be noted that the effects of damage on the propagating waves are small compared to the effects due to the geometry of the finite structure itself which causes dispersion (phase modulation) and scattering of waves. In order to extract a meaningful information about the damage parameter from the signals and also to remove baseline noise due to boundary scattering, we employ time–frequency analysis in this paper. In the time–frequency plane, the arrivals of the scattered waves, generated by the presence of damage, are identified in term of arrival time, which is a function of the group speed. Hence with the help of arrival time information and frequency dependent group speed from dispersion curves, it is possible to estimate the damage location. Quek et al. used time–frequency methods like wavelet transform (WT) [9] and Hilbert–Huang transform (HHT) for detecting the location of the damage from experimental signals [10]. However, extracting more number of quantitative estimates regarding damage size and its structural influence are challenging tasks. We address some of the related issues in the following sections.

2. Time–frequency analysis

A wide variety of signal processing methods are currently available, namely the time-series analysis, the frequency analysis and the time–frequency analysis. Time-series methods cannot separate defect scattered composition appropriately from a raw signal containing frequency/wavelength sensitive features over multiple frequencies. In the frequency domain analysis, we loose the time information such as arrival time, dispersion, etc. These problems compel one to combine the time-domain information with the frequency domain information resulting in time–frequency analysis. A time–frequency representation (TFR) of a signal provides information about how the spectral content of the signal evolves with time, thus providing an ideal tool to

analyze and interpret non-stationary signals. This is performed by mapping a one-dimensional signal from the time domain to a two-dimensional time–frequency space. A variety of methods for obtaining the energy density of a function, simultaneously in the time and frequency have been developed, most notably the short time Fourier transform (STFT), Wigner–Ville distribution (WVD), WT and HHT.

2.1. Short time Fourier transform (STFT)

The STFT is a modified version of the Fourier transform [11]. In STFT, the non-stationary signal is divided into small segments, which are assumed to be stationary. This is done using a window function of a chosen width. The window is shifted and multiplied with the signal to obtain the set of stationary signals. Fourier transform is then applied to each of these short window signals. One can write

$$\hat{f}(\omega, \tau)_{\text{STFT}} = \int_{-\infty}^{+\infty} f(t)g(t - \tau)e^{-j\omega t}\,dt, \tag{1}$$

where $f(t)$ is the signal analysed, $g(t)$ is a window function, $\hat{f}$ indicates the transformed signal, ω is the angular frequency and τ is a parameter for translation along time axis. In STFT, once the window has been chosen the time–frequency resolution is constant throughout the time–frequency plane.

2.2. Wavelet transform (WT)

The WT was introduced by a French geophysicist Morlet in the early 1980 to study seismic signals [12]. Later Grossmann, Meyer, Mallat and Daubechies established a proper mathematical foundation for wavelets [13]. Since then, wavelets have been extensively employed in signal processing applications. In WT, a varying window function is used, which can be dilated and compressed and is called the mother wavelet. A wavelet is defined using two parameters: a scaling parameter a, which is the inverse of frequency, and a translation parameter b, which translates the window function along the time axis. The continuous WT of a signal $f(t)$ is given by

$$\hat{f}(a, b)_{\text{WT}} = \frac{1}{\sqrt{a}} \int_{-\infty}^{+\infty} f(t)\psi^*\left(\frac{t - b}{a}\right)e^{-j\omega t}\,dt, \tag{2}$$

where ψ is the wavelet function. WT overcomes the resolution problem of STFT by letting the resolution of both the time and the frequency vary in the time–frequency plane in order to obtain a multiresolution map.

2.3. Hilbert–Huang transform (HHT)

The HHT proposed by Huang et al. [14] is suitable for analysing both nonlinear and non-stationary signals in the time–frequency plane. HHT consists of two parts, one is the empirical mode decomposition (EMD) and the other part is the Hilbert transform (HT). The objective behind EMD is to decompose a measured response signal $x(t)$ into intrinsic mode functions (IMFs) that admit well-behaved HT. It has been shown by Huang et al. [14] that the characteristics of the signal can be extracted through the behaviour of the IMFs, where the first IMF has the highest frequency contents of the signal. The instantaneous frequency is obtained by applying HT to each IMF obtained from EMD. The HT of a signal $x(t)$ is given by

$$y(t) = \text{HT}(x(t)) = \frac{1}{\pi}\text{PV}\int_{-\infty}^{+\infty}\frac{x(\tau)}{t - \tau}\,d\tau, \tag{3}$$

in which PV indicates the cauchy principal value of the singular integral. A complex analytic signal $z(t)$ is then formed as

$$z(t) = x(t) + iy(t) = a(t)e^{i\theta(t)}, \tag{4}$$

where $a(t) = \sqrt{x^2 + y^2}$ and $\theta(t) = \tan^{-1}(y/x)$. Here, $a(t)$ is the instantaneous amplitude, θ is the phase function and the instantaneous frequency is $\omega = d\theta/dt$. The limitations in the above steps are that they do not

have a proper mathematical basis compared to other time–frequency analysis. Also there are numerical convergence issues in getting the IMFs.

Jeong and Jang [15] constructed dispersion curves for thin composite plates by applying WT. The group velocity computed at different frequencies were used to locate the acoustic emission source location. Prosser et al. [16] used WVD to study dispersion of lamb waves in composite plates. The drawback of WVD compared to other TFR methods is the presence of cross-energy terms and these terms make time–frequency analysis difficult. Paget et al. [17] embedded PZT sensors in composites and conducted experiments to study damages like delamination, impact damage and sawcut damage. In that work WT was used to study the experimental signals and damages were differentiated by looking at the wavelet coefficients. Ip et al. [18] used the Gabor wavelet to extract the dominant wave group from the measured acceleration signals. The wave speed of the fundamental antisymmetrical Lamb wave mode (A_0) mode in an aluminium beam was determined and flexural modulus was computed in that work.

Pines et al. [19] used HHT for structural health monitoring of civil structures. Vibration signals were studied in the above work using HHT and the changes in frequency and magnitude were used to characterise the damage in the structure. Vibration based damage detection in composite wingbox structure using HHT was proposed by Chen et al. [20]. It was found that in HHT, serious problems of the spline fitting can occur near the end points, where the cubic spline fitting can have large swings. These end swings can eventually propagate inward during EMD and corrupt the whole data, especially in the low frequency band [14]. Chen et al. analysed the problem of end effects in HHT and proposed a method to overcome it. TFR analysis of transient dispersive waves was carried out by Apostoloudia et al. [21]. They compared the performance of WVD, WT and HHT by analysing the flexural waves in beams subjected to an impact load. Most of the published literature involving HHT are related to the study of vibration problems and very few work has been reported using HHT to study high frequency acoustic and ultrasonic scattering in composite structures.

The main focus of this paper is to provide useful mathematical and computational insight into the problem of damage detection in composite structures based on wave propagation technique. The paper aims to use time–frequency analysis for characterisation of damages in composites, namely, (1) identifying localised damages and (2) dispersion of multifrequency signal after they interact with different types of damages. The effectiveness of the two TFR methods, namely WT and HHT, are investigated. The focus here is to compare their ability in quantifying damage by analysing experimental and simulated signals from damage.

3. A comparative view of various time–frequency analysis

Even though both STFT and WT have proper mathematical representation, they have the drawback of having non-adaptive basis. Other problems are the energy leakage and the presence of cross-energy terms in the energy distribution in the time–frequency plane for both STFT and WT coefficients. STFT and WT are linear transforms, whereas their energy representations are always nonlinear in nature. The cross-terms that exist in the energy distribution of both WT and STFT for a multicomponent signal are comparable with those found in WVD. Consider a signal $\bar{x}$ such that

$$\bar{x}(t) = x_1(t) + x_2(t),\tag{5}$$

where $x_1(t)$ and $x_2(t)$ are the components of the signal. STFT of signal $\bar{x}$ is given by

$$\hat{\bar{x}}(\omega, \tau)_{\text{STFT}} = \hat{x}_1(\omega, \tau)_{\text{STFT}} + \hat{x}_2(\omega, \tau)_{\text{STFT}}.\tag{6}$$

Now, let us consider the energy distribution of $\hat{\bar{x}}$, which is given by

$$\begin{aligned}
|\hat{\bar{x}}(\omega, \tau)_{\text{STFT}}|^2 &= |\hat{x}_1(\omega, \tau)_{\text{STFT}} + \hat{x}_2(\omega, \tau)_{\text{STFT}}|^2\\
&= [|\hat{x}_1(\omega, \tau)_{\text{STFT}}|^2 + |\hat{x}_2(\omega, \tau)_{\text{STFT}}|^2]_{\text{autocomponent}}\\
&\quad + 2\,\text{Re}[\hat{x}_1(\omega, \tau)_{\text{STFT}}\hat{x}_2^*(\omega, \tau)_{\text{STFT}}]_{\text{cross-component}}\\
&= |\hat{x}_1(\omega, \tau)_{\text{STFT}}|^2 + |\hat{x}_2(\omega, \tau)_{\text{STFT}}|^2\\
&\quad + 2|\hat{x}_1(\omega, \tau)_{\text{STFT}}||\hat{x}_2(\omega, \tau)_{\text{STFT}}|\cos[\phi_{x_1}(\omega, \tau) - \phi_{x_2}(\omega, \tau)],
\end{aligned}\tag{7}$$

where $\hat{x}_2^*(\omega,\tau)_{\text{STFT}}$ is the complex conjugate of $\hat{x}_2(\omega,\tau)_{\text{STFT}}$, $|\hat{x}(\omega,\tau)_{\text{STFT}}|$ and $\phi(\omega,\tau)$ are the magnitude and phase, respectively. The magnitude and the phase constitute the spectogram. The first two terms correspond to the squared magnitude of the STFT autocomponents, whereas the last term is the cross-component. In general, for a multicomponent signal $\bar{x}(t) = \sum_{i=1}^{n} x_i(t)$ the energy distribution of $\hat{\bar{x}}(\omega,\tau)_{\text{STFT}}$ can be expressed as

$$|\hat{\bar{x}}(\omega,\tau)_{\text{STFT}}|^2 = \sum_{i=1}^{n} |\hat{\bar{x}}_i(\omega,\tau)_{\text{STFT}}|^2 + 2\sum_{k=1}^{n-1}\sum_{l=k+1}^{n} |\hat{x}_k(\omega,\tau)_{\text{STFT}}||\hat{x}_l(\omega,\tau)_{\text{STFT}}|\cos[\phi_{x_k}(\omega,\tau) - \phi_{x_l}(\omega,\tau)]. \quad (8)$$

Similarly for a multicomponent signal, the energy distribution of $\hat{\bar{x}}(a,b)_{\text{WT}}$ is given by

$$|\hat{\bar{x}}(a,b)_{\text{WT}}|^2 = \sum_{i=1}^{n} |\hat{\bar{x}}_i(a,b)_{\text{WT}}|^2 + 2\sum_{k=1}^{n-1}\sum_{l=k+1}^{n} |\hat{x}_k(a,b)_{\text{WT}}||\hat{x}_l(a,b)_{\text{WT}}|\cos[\phi_{x_k}(a,b) - \phi_{x_l}(a,b)]. \quad (9)$$

The cross-terms for the WT and the STFT occur at the intersection of their respective WT and STFT spaces [22]. The parameters of the cross-terms are a function of the difference in the central frequencies and central times of the perpended signals. The amplitude of the cross-terms can be as large as twice the product of the magnitude of the transforms of the individual components of the signal. The cross-terms in Eqs. (9) and (10) are functions of the product $|\hat{x}_k(\omega,\tau)_{\text{STFT}}||\hat{x}_l(\omega,\tau)_{\text{STFT}}|$ and $|\hat{x}_k(a,b)_{\text{WT}}||\hat{x}_l(a,b)_{\text{WT}}|$, respectively. This product will be zero if $|\hat{x}_k(\omega,\tau)_{\text{STFT}}|$ and $|\hat{x}_l(\omega,\tau)_{\text{STFT}}|$ (for WT $|\hat{x}_k(a,b)_{\text{WT}}|$ and $|\hat{x}_l(a,b)_{\text{WT}}|$) have non-overlapping supports. To show the influence of the cross-terms in the energy distributions of both STFT and WT, let us consider an analytical signal

$$x(t) = \cos 2\pi(500t) + \cos 2\pi(1500t).$$

The energy distributions of the signal using STFT and WT are shown in Figs. 1 and 2. In the example, we have chosen a hamming window for STFT and Morlet wavelet for WT to analyse the multicomponent signal.
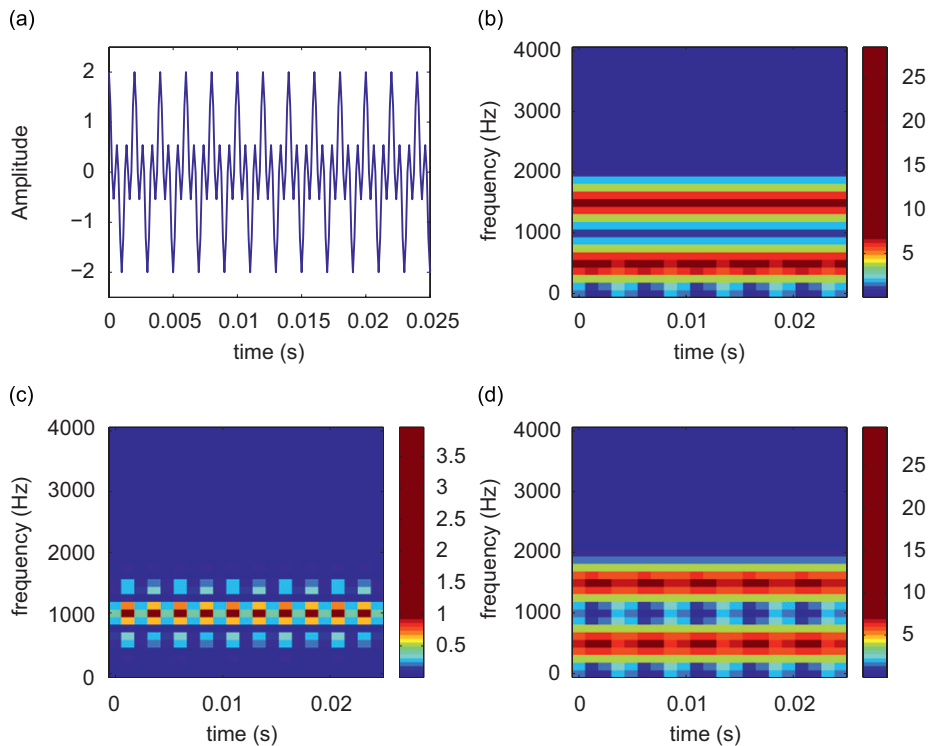

Fig. 1. STFT energy distribution: (a) signal $x(t) = \cos(2\pi(500t)) + \cos(2\pi(1500t))$; (b) autocomponents; (c) cross-components; (d) spectogram with $T = 2.5\,\text{ms}$.
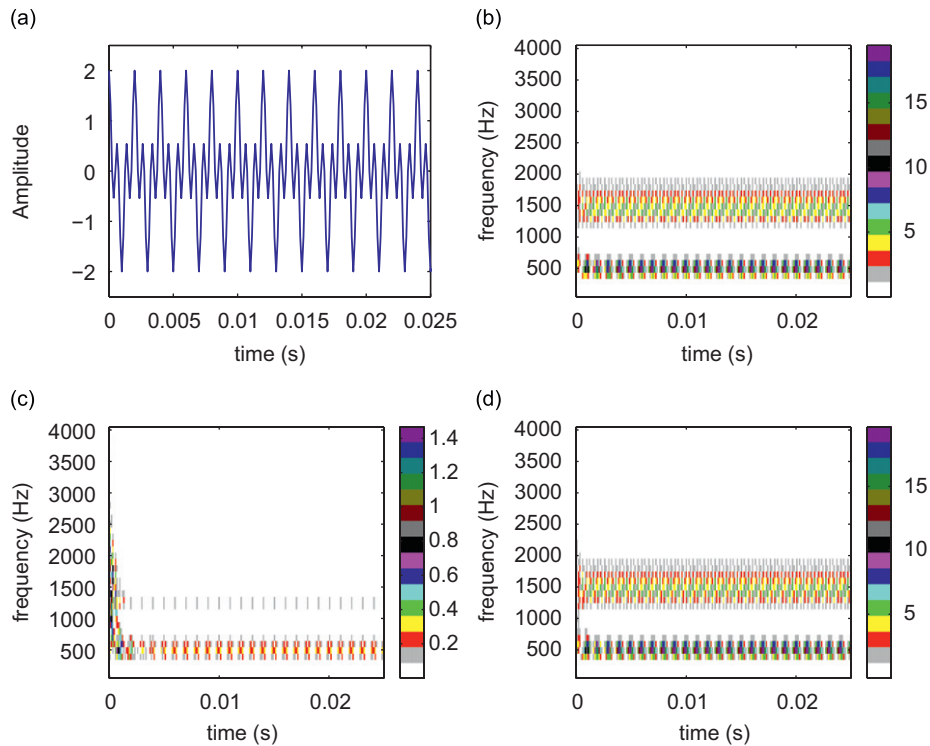
Fig. 2. WT energy distribution: (a) signal $x(t) = \cos(2\pi(500t)) + \cos(2\pi(1500t))$; (b) autocomponents; (c) cross-components; (d) scalogram.

The window or the wavelet functions affect the concentration of the autoterms in the signal and the overlap between them shown in Figs. 1 and 2 leads to the cross-terms. The presence of cross-terms in the energy distributions affects the time–frequency localisation, thus resulting in energy leakage. The existence of cross-term depends on the nature of the multicomponent signal and the choice of window or wavelet functions. These cross-term contributions have to be minimised in order to have an accurate time–frequency localisation.

3.1. Advantages and limitations of HHT

STFT and WT are suitable for studying only linear and non-stationary signals. Both STFT and WT use a single window function or *a priori* chosen basis to analyse the entire signal and hence making themselves non-adaptive in nature. This problem is overcome by HHT [14], which is suitable for analysing both nonlinear and non-stationary signals in the time–frequency plane. The adaptive nature of HHT makes it superior compared to other methods of time–frequency analysis.

The method or the idea of EMD in HHT is faced with a fundamental difficulty of not admitting an analytical definition, but of being rather described by the algorithm, thus making the analysis of its performance difficult. The EMD algorithm consists of the following important issues (a) extrema locations (b) extrema interpolation (c) end effects (d) sifting and stopping criterion [23]. The EMD algorithm generally operates on real space and discrete time signals. If the time signal is not sampled properly, the extremas may fall in between the sampling points. This problem can be solved by oversampling the signal. We use cubic spline function to interpolate between the extrema points and construct the IMF. Such an interpolation scheme introduces overshoots in order to achieve continuous second-order derivatives at the extrema points. These effects introduce new extrema points that should have not been present in the original signal or shifting of the extrema points to another location. As a result, it introduces new high frequencies at false positions in the signal. Another problem with cubic spline is its poor behaviour at the end points of the signals. The end effects surface when one has to decide what to do with the first and the last samples. The drawback of using
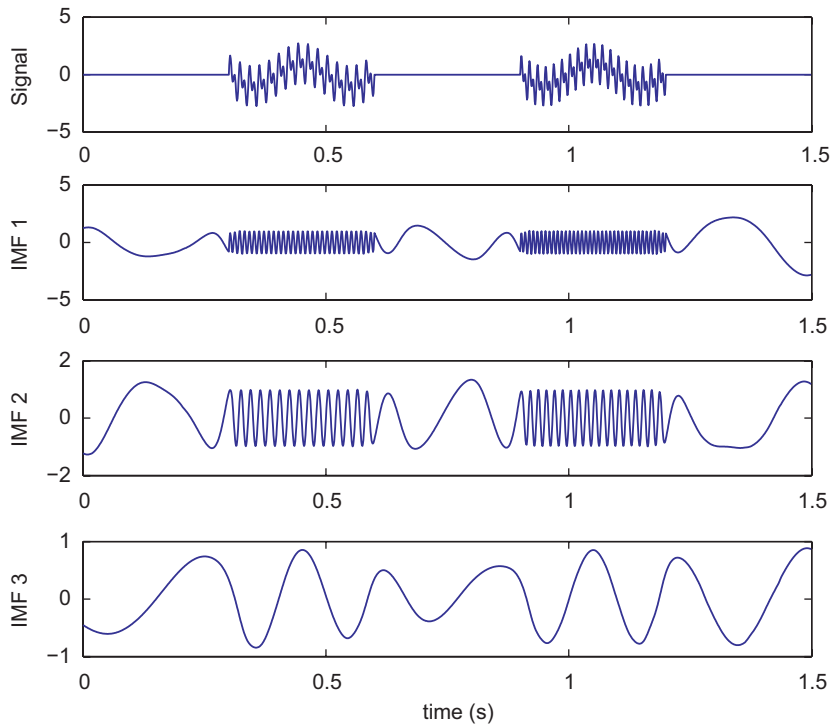
Fig. 3. End effects while using cubic splines.

spline function for interpolation and the end effects of EMD is demonstrated next by analysing the following signal:

$$x(t) = \begin{cases} 0, & 0 \leqslant t < 0.3, \\ \sin(10\pi t) + \sin(100\pi t) + \sin(200\pi t), & 0.3 \leqslant t < 0.6, \\ 0, & 0.6 \leqslant t < 0.9, \\ \sin(10\pi t) + \sin(120\pi t) + \sin(240\pi t), & 0.9 \leqslant t < 1.2, \\ 0, & 1.2 \leqslant t < 1.5. \end{cases}$$

This signal and its IMFs are shown in Fig. 3. The first and the last samples are not subjected to any end conditions and this results in oscillations near the end. The problem of end effect can be overcome by imposing certain conditions in the end samples. The spline approximation used for the computation of the envelopes resulted in the introduction of new extrema points in the region where the signal is constant. Fig. 3 illustrates the problem of end effects and introduction of new frequencies in the IMFs due to spline approximation obtained using EMD. Another problem is the stopping criterion to obtain the IMFs. If the stopping criterion is not properly satisfied, the IMF cannot be computed properly and this will affect the computation of IMFs.

4. Modelling and simulation of elastic wave scattering due to damages

Efficient models are required to understand the elastic wave dispersion and scattering in structures. In the literature two different spectral element approaches are reported for wave propagation modelling. The first one is based on the fast Fourier transformation (FFT) [24], whereas the second one is the time-domain method [25]. The first spectral method popularised by Doyle [24], is a fast Fourier transform based method with the matrix structure of finite element method (FEM). Typically, a single element is sufficient to model wave propagation in large uniform structures. The second spectral method [26,27] combines the accuracy of spectral methods with the flexibility of the FEM to model wave propagation. In this paper Fourier spectral finite

element method is employed for efficient computation of elastic wave scattering in structures. By virtue of its domain transfer formulation and fast fourier transform, it bypasses the large system size of *hp*-FEM. The basic framework of spectral finite element model employed in the present paper can be found in Ref. [24] for isotropic solid and in Refs. [1,2,28] for laminated composite. SFEM is found to be suitable for damage identification and characterisation problems and we will make use of this method in formulating various parameterised models of wave scattering from damage, followed by signal analysis using STFT, WT and HHT.

5. Spectral finite element for modelling of elastic wave propagation in composite beams

Substituting the displacement field variables in the governing differential equations for a particular wave propagation problem (see [2,29]), one obtains the characteristic equation in the frequency-wavenumber (ω, k) space

$$u(x,t) = \sum_{n=1}^{N} \tilde{u}_j e^{-i(k_j x - \omega_n t)}, \quad [\hat{F}(k_j, \omega_n)]\{\tilde{u}_j\} = \{0\}, \tag{10}$$

where u is the displacement, $\tilde{u}_j$ is the wave amplitude. This yields a sixth-order characteristic equation in k_j given by

$$\det[\hat{\mathbf{F}}(k_j, \omega_n)] = 0, \quad \forall \omega_n, \ n = 1, 2, \ldots, N. \tag{11}$$

Procedure to solve this equation in order to find the wavenumbers $k_j(\omega_n)$ can be found in Refs. [2,28–30]. In the following sections, we shall use the notation $(\hat{\cdot})$ for fourier transformed quantities and $(\tilde{\cdot})$ for its amplitude (wave coefficients).

5.1. Spectral finite element modelling approach

In this approach, one is able to utilise the dispersion branches over a suitably broad frequency band. After computing the wavenumbers $k_j(\omega_n)$ for a particular sampling frequency ω_n, the generic displacement vector is written as

$$\hat{u}(x, \omega_n) = \begin{bmatrix} R_{11} & \ldots & R_{16} \\ R_{21} & \ldots & R_{26} \\ R_{31} & \ldots & R_{36} \end{bmatrix} [\mathbf{\Lambda}'] \begin{Bmatrix} \tilde{u}_1 \\ \vdots \\ \tilde{u}_6 \end{Bmatrix} = T'(x, \omega_n)\tilde{u}, \tag{12}$$

where $[\mathbf{\Lambda}']$ is a diagonal matrix with exponential entries $(e^{-ik_j x})$ [5].

By evaluating Eq. (12) at the element nodes at $x = 0, L$ (for one-dimensional element) the element nodal displacement vector can be expressed as

$$\hat{\mathbf{u}}^e = \begin{bmatrix} \mathbf{T}'(x, \omega_n)_{x=0} \\ \mathbf{T}'(x, \omega_n)_{x=L} \end{bmatrix} \tilde{\mathbf{u}} = \mathbf{T}''\tilde{\mathbf{u}}. \tag{13}$$

The non-singular complex matrix $\mathbf{T}''$ represents the local wave characteristics of the displacement field. Eliminating the unknown wave coefficient amplitude vector $\tilde{\mathbf{u}}$ from Eq. (12) using Eq. (13), the generic displacement field $\hat{u}(x, \omega_n)$ can be expressed in terms of the nodal displacements as

$$\hat{\mathbf{u}}(x, \omega_n) = \mathbf{T}'(x, \omega_n)\mathbf{T}''^{-1}\hat{\mathbf{u}}^e = \bar{\mathbf{N}}(x, \omega_n)^e\hat{\mathbf{u}}^e, \tag{14}$$

where $\bar{\mathbf{N}}(x, \omega_n)$ is the exact/enriched spectral element shape function matrix. Next, the natural boundary conditions are evaluated for $x = 0, L$, which yield the element nodal force vector $\hat{\mathbf{f}}^e$ as

$$\hat{\mathbf{f}}^e(\omega_n) = \begin{bmatrix} -\mathbf{Q}'\mathbf{R}\mathbf{\Lambda}'_{x=0} - \mathbf{Q}''\mathbf{R}\mathbf{\Lambda}''_{x=0} \\ \mathbf{Q}'\mathbf{R}\mathbf{\Lambda}'_{x=L} + \mathbf{Q}''\mathbf{R}\mathbf{\Lambda}''_{x=L} \end{bmatrix} \mathbf{T}''^{-1}\hat{\mathbf{u}}^e(\omega_n) = \hat{\mathbf{K}}^e(\omega_n)\hat{\mathbf{u}}^e(\omega_n), \tag{15}$$

where $\hat{\mathbf{K}}^e(\omega_n)$ is the exact spectral finite element stiffness matrix and it is a complex matrix function of frequency unlike the form $-\omega^2\mathbf{M} + \mathbf{K}$ as obtained via hp-FEM. $\mathbf{Q}'$ and $\mathbf{Q}''$ are both real matrices whose entries are the functions of the cross-sectional stiffness. $\mathbf{\Lambda}''$ is a diagonal matrix obtained as

$$\mathbf{\Lambda}''_{jj} = \frac{\partial}{\partial x}\mathbf{\Lambda}'_{jj}. \tag{16}$$

For those kinematics (e.g., higher-order beam, plate and layered system) where the complete wave vector is to be considered instead of a scalar wavenumber as in case of simple beam, it is not always possible to construct an exact spectral element. However, it is possible to construct an enriched spectral element using incomplete dispersion characteristics [31]. In the next section we discuss the SFEMs for delamination and material degradation due to matrix cracks. In the end of this paper we employ such parametric models for damage identification studies.

6. Delaminated beams

The location of the nodes of the spectral elements for a delaminated beam is shown in Fig. 4a. In absence of delamination, one spectral element between nodes 1 and 2 is sufficient. This is of great advantage that a very small system is to be solved while adopting a suitable parameter estimation scheme like neural network, genetic algorithm, etc. The presence of delamination, when treated as structural discontinuity by neglecting the effect of stress singularity at the delamination tip, increases the number of elements from one to four. Six more nodes are introduced to model individual base-laminates and sub-laminates. For the sub-laminate-elements (elements 3 and 4) the nodes are located at the mid-plane of the sub-laminates and element lengths are equal to the length of the delamination. The kinematic assumption for the interface of base-laminate and sub-laminates is that the cross-section remains straight, that is, the slope is continuous and constant at the interface. Under this assumption, one obtains the following kinematic relationship between the nodal degrees of freedom:

$$\hat{\mathbf{u}}_3 = \left\{ \begin{array}{c} \hat{u}_3^0 \\ \hat{w}_3 \\ \hat{\phi}_3 \end{array} \right\} = \left\{ \begin{array}{c} \hat{u}_4^0 + h_2\hat{\phi}_4 \\ \hat{w}_4 \\ \hat{\phi}_4 \end{array} \right\} = \begin{bmatrix} 1 & 0 & h_2 \\ 0 & 1 & 0 \\ 0 & 0 & 1 \end{bmatrix} \left\{ \begin{array}{c} \hat{u}_4^0 \\ \hat{w}_4 \\ \hat{\phi}_4 \end{array} \right\} = \mathbf{S}'\hat{\mathbf{u}}_4, \tag{17}$$
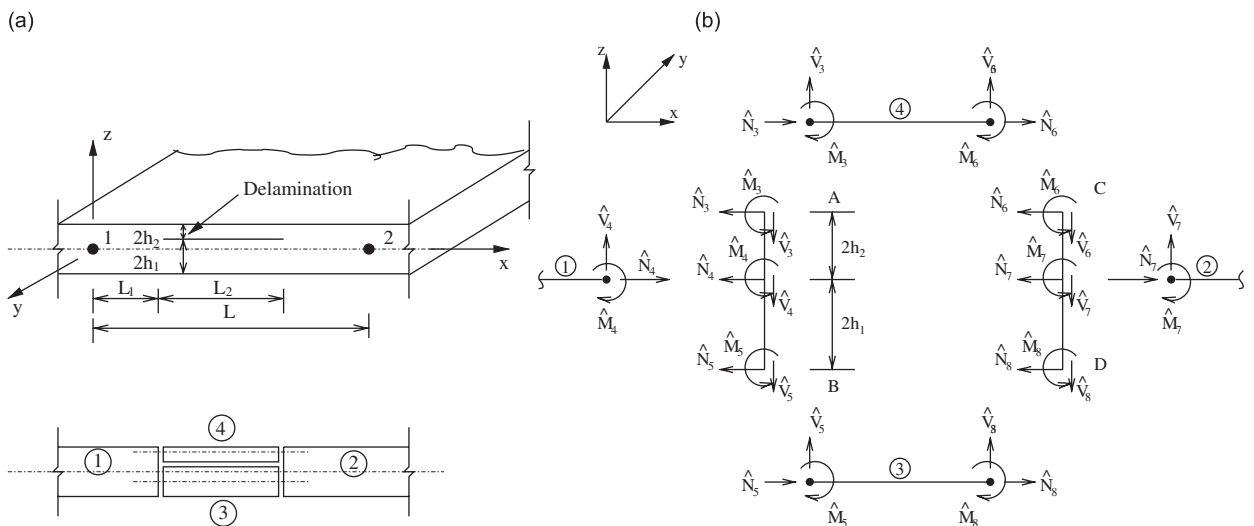

Fig. 4. (a) Modelling of an embedded delamination with base-laminates and sub-laminates (one-dimensional waveguide). Waveguide 1–2: base-laminates; waveguide 3–4: sub-laminates. (b) Force balance at the interface between base-laminate and sub-laminate elements.

$$\hat{\mathbf{u}}_5 = \left\{ \begin{array}{c} \hat{u}_5^0 \\ \hat{w}_5 \\ \hat{\phi}_5 \end{array} \right\} = \left\{ \begin{array}{c} \hat{u}_4^0 - h_2\hat{\phi}_4 \\ \hat{w}_4 \\ \hat{\phi}_4 \end{array} \right\} = \begin{bmatrix} 1 & 0 & -h_2 \\ 0 & 1 & 0 \\ 0 & 0 & 1 \end{bmatrix} \left\{ \begin{array}{c} \hat{u}_4^0 \\ \hat{w}_4 \\ \hat{\phi}_4 \end{array} \right\} = \mathbf{S}''\hat{\mathbf{u}}_4 \tag{18}$$

and similarly,

$$\hat{\mathbf{u}}_6 = \mathbf{S}'\hat{\mathbf{u}}_7, \quad \hat{\mathbf{u}}_8 = \mathbf{S}''\hat{\mathbf{u}}_7. \tag{19}$$

For the equilibrium of forces at the left interface AB (Fig. 4(b)), one can derive the following force balance equation in frequency domain as

$$\left\{ \begin{array}{c} \hat{N}_4(\omega_n) \\ \hat{V}_4(\omega_n) \\ \hat{M}_4(\omega_n) \end{array} \right\} + \left\{ \begin{array}{c} \hat{N}_3(\omega_n) \\ \hat{V}_3(\omega_n) \\ \hat{M}_3(\omega_n) \end{array} \right\} + \left\{ \begin{array}{c} 0 \\ 0 \\ h_2\hat{N}_3(\omega_n) \end{array} \right\} + \left\{ \begin{array}{c} \hat{N}_5(\omega_n) \\ \hat{V}_5(\omega_n) \\ \hat{M}_5(\omega_n) \end{array} \right\} + \left\{ \begin{array}{c} 0 \\ 0 \\ -h_1\hat{N}_5(\omega_n) \end{array} \right\} = \left\{ \begin{array}{c} 0 \\ 0 \\ 0 \end{array} \right\}, \tag{20}$$

where $\hat{N}, \hat{V}, \hat{M}$ stand for frequency domain axial force, shear force and bending moment, respectively. Eq. (20) can be rewritten in matrix form as

$$\hat{\mathbf{f}}_4 + \mathbf{S}_1^T\hat{\mathbf{f}}_3 + \mathbf{S}''^T\hat{\mathbf{f}}_5 = \mathbf{0}. \tag{21}$$

Similarly, from the equilibrium of the right interface CD, one has

$$\hat{\mathbf{f}}_7 + \mathbf{S}'^T\hat{\mathbf{f}}_6 + \mathbf{S}''^T\hat{\mathbf{f}}_8 = \mathbf{0}. \tag{22}$$

After a finite element assembly of Eqs. (15), (21) and (22), one has the global system equation:

$$\begin{bmatrix} \hat{\mathbf{K}}_{11}^{(1)} & \hat{\mathbf{K}}_{12}^{(1)} & 0 & 0 \\ \hat{\mathbf{K}}_{21}^{(1)} & \begin{pmatrix} \hat{\mathbf{K}}_{22}^{(1)} + \mathbf{S}'^T\hat{\mathbf{K}}_{11}^{(4)}\mathbf{S}' \\ +\mathbf{S}''^T\hat{\mathbf{K}}_{11}^{(3)}\mathbf{S}'' \end{pmatrix} & \begin{pmatrix} \mathbf{S}'^T\hat{\mathbf{K}}_{12}^{(4)}\mathbf{S}' \\ +\mathbf{S}''^T\hat{\mathbf{K}}_{12}^{(3)}\mathbf{S}'' \end{pmatrix} & 0 \\ 0 & (\mathbf{S}'^T\hat{\mathbf{K}}_{21}^{(4)}\mathbf{S}' + \mathbf{S}''^T\hat{\mathbf{K}}_{21}^{(3)}\mathbf{S}'') & \begin{pmatrix} \hat{\mathbf{K}}_{11}^{(2)} + \mathbf{S}'^T\hat{\mathbf{K}}_{22}^{(4)}\mathbf{S}' \\ +\mathbf{S}''^T\hat{\mathbf{K}}_{22}^{(3)}\mathbf{S}'' \end{pmatrix} & \hat{\mathbf{K}}_{12}^{(2)} \\ 0 & 0 & \hat{\mathbf{K}}_{21}^{(2)} & \hat{\mathbf{K}}_{22}^{(2)} \end{bmatrix} \times \left\{ \begin{array}{c} \hat{\mathbf{u}}_1 \\ \hat{\mathbf{u}}_4 \\ \hat{\mathbf{u}}_7 \\ \hat{\mathbf{u}}_2 \end{array} \right\} = \{\hat{\mathbf{f}}_1 \ 0 \ 0 \ \hat{\mathbf{f}}_2\}^T. \tag{23}$$

Performing stationary condensation at each sampling frequency (ω_n) for the degrees of freedom at the internal nodes 4 and 7, the final form of the equilibrium equation for this delaminated beam is obtained as

$$\hat{\tilde{\mathbf{K}}}(\omega_n)\left\{ \begin{array}{c} \hat{\mathbf{u}}_1(\omega_n) \\ \hat{\mathbf{u}}_2(\omega_n) \end{array} \right\} = \left\{ \begin{array}{c} \hat{\mathbf{f}}_1(\omega_n) \\ \hat{\mathbf{f}}_2(\omega_n) \end{array} \right\}, \tag{24}$$

where $\hat{\tilde{\mathbf{K}}}$ is the effective dynamic stiffness matrix for the *spectral element with embedded delamination*. Now, one only needs to replace an usual spectral element with this *damage spectral element* wherever a possible delamination may exist, keeping the original FE mesh unaltered. The parameters hidden inside are (h_1, h_2, L_1, L_2), see Fig. 4. Hence, it is evident that insertion of this parameterised element on a modular approach is very much suitable for faster modelling and simulation.

7. Beam with degraded material constants

In most of the damage models reported in literature, where the transverse matrix cracks, fiber splitting, delamination, etc. and combination of them are considered, the degradation of effective elastic moduli of damaged laminates can be used as damage parameters. Once estimated through measured signal and model based solution, such parameters can further be correlated to the damage states and residual life of the structure. Degraded laminate constitutive law under the plane-stress or the plane-strain condition can be
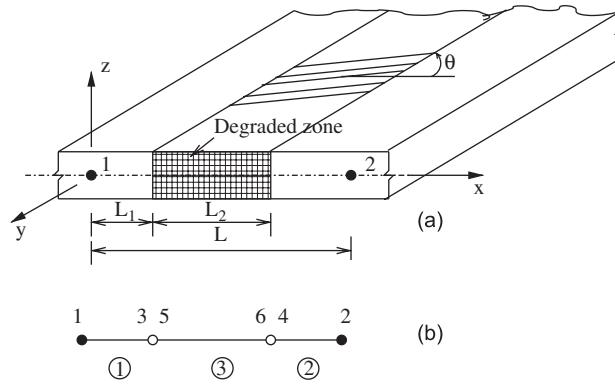
Fig. 5. (a) Composite beam segment with the degraded zone of size L_2. The whole segment is represented by the end nodes 1 and 2 of the spectral element. (b) The element local configuration showing the internal element numbers (1), (2) and (3) by circles and the associated nodes 1–3, 2–4, and 5–6.

expressed as [4]

$$\begin{Bmatrix} \sigma_{xx} \\ \sigma_{zz} \\ \tau_{xz} \end{Bmatrix} = \begin{bmatrix} \alpha_{11}Q_{11} & \alpha_{13}Q_{13} & 0 \\ \alpha_{13}Q_{13} & \alpha_{33}Q_{33} & 0 \\ 0 & 0 & \alpha_{55}Q_{55} \end{bmatrix} \begin{Bmatrix} \varepsilon_{xx} \\ \varepsilon_{zz} \\ \gamma_{xz} \end{Bmatrix}, \tag{25}$$

where z is the laminate thickness direction and x is the longitudinal direction ($0°$ fiber direction), α_{ij} are the degradation factors. For undamaged laminates $\alpha_{ij} = 1$. In general α_{ij} are functions of micro-crack geometries and growth mechanism [4].

The location of the two nodes of the spectral element with embedded degraded zone in a beam is shown in Fig. 5(a). In absence of degradation, one spectral element between nodes 1 and 2 is sufficient. The presence of degradation, when treated as structural discontinuity by neglecting the effect of stress singularity at the delamination tip, increases the number of elements from one to three as shown in Fig. 5(b). In usual hp-finite element approach, one has to refine the mesh or enrich the interpolation drastically in the degraded zone. Here only four more nodes are introduced to model the degraded zone (element (3)) and the surrounding undamaged zones (elements (1) and (2)).

The kinematic assumption of continuity of displacements and rotations at the internal element nodes 3, 5 and 4, 6 leads to the following:

$$\hat{\mathbf{u}}_5 = \{\hat{u}_5^0 \ \ \hat{w}_5 \ \ \hat{\phi}_5\}^{\mathrm{T}} = \hat{\mathbf{u}}_3, \quad \hat{\mathbf{u}}_6 = \{\hat{u}_6^0 \ \ \hat{w}_6 \ \ \hat{\phi}_6\}^{\mathrm{T}} = \hat{\mathbf{u}}_4. \tag{26}$$

From the equilibrium of the nodal forces and the moments at the left interface (between nodes 3 and 5) and at the right interfaces (between nodes 4 and 6), we get, respectively,

$$\hat{\mathbf{f}}_3 + \hat{\mathbf{f}}_5 = \mathbf{0}, \quad \hat{\mathbf{f}}_4 + \hat{\mathbf{f}}_6 = \mathbf{0}. \tag{27}$$

Following Eq. (15), the finite element equilibrium equation for the jth internal element ($j = 1, 2, 3$) with nodes p and q is written as

$$\begin{bmatrix} \hat{\mathbf{K}}_{11}^{(j)} & \hat{\mathbf{K}}_{12}^{(j)} \\ \hat{\mathbf{K}}_{21}^{(j)} & \hat{\mathbf{K}}_{22}^{(j)} \end{bmatrix} \begin{Bmatrix} \hat{\mathbf{u}}_p \\ \hat{\mathbf{u}}_q \end{Bmatrix} = \begin{Bmatrix} \hat{\mathbf{f}}_p \\ \hat{\mathbf{f}}_q \end{Bmatrix}. \tag{28}$$
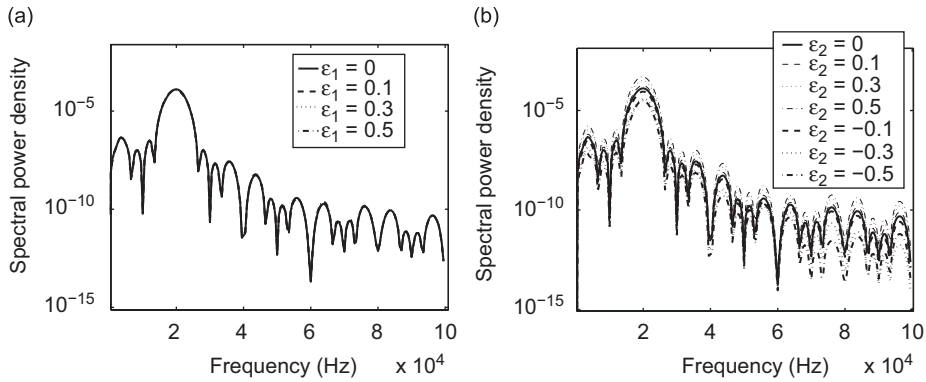
(a)

(b)

Fig. 6. Spectral power density for: (a) various ε_1, $\varepsilon_2 = 0$; (b) various ε_2, $\varepsilon_1 = 0$ (numerical example in Section 8.1).

Performing finite element assembly of Eq. (28) over the three internal elements (1), (2) and (3) (see Fig. 6), we get

$$
\begin{bmatrix}
\hat{\mathbf{K}}_{11}^{(1)} & \hat{\mathbf{K}}_{12}^{(1)} & \mathbf{0} & \mathbf{0} \\
\hat{\mathbf{K}}_{21}^{(1)} & \hat{\mathbf{K}}_{22}^{(1)} + \hat{\mathbf{K}}_{11}^{(2)} & \hat{\mathbf{K}}_{12}^{(2)} & \mathbf{0} \\
\mathbf{0} & \hat{\mathbf{K}}_{21}^{(2)} & \hat{\mathbf{K}}_{22}^{(2)} + \hat{\mathbf{K}}_{11}^{(3)} & \hat{\mathbf{K}}_{12}^{(3)} \\
\mathbf{0} & \mathbf{0} & \hat{\mathbf{K}}_{21}^{(3)} & \hat{\mathbf{K}}_{22}^{(3)}
\end{bmatrix}_{(12 \times 12)}
\begin{Bmatrix}
\hat{\mathbf{u}}_1 \\
\hat{\mathbf{u}}_3 \\
\hat{\mathbf{u}}_4 \\
\hat{\mathbf{u}}_2
\end{Bmatrix}
=
\begin{Bmatrix}
\hat{\mathbf{f}}_1 \\
\mathbf{0} \\
\mathbf{0} \\
\hat{\mathbf{f}}_2
\end{Bmatrix}.
\tag{29}
$$

Next, by performing stationary condensation at each sampling frequency ω_n at the internal nodes 3 and 4 and assuming that no load is applied on the damaged zone, Eq. (29) becomes

$$
\hat{\tilde{\mathbf{K}}}(\omega_n)
\begin{Bmatrix}
\hat{\mathbf{u}}_1(\omega_n) \\
\hat{\mathbf{u}}_2(\omega_n)
\end{Bmatrix}
=
\begin{Bmatrix}
\hat{\mathbf{f}}_1(\omega_n) \\
\hat{\mathbf{f}}_2(\omega_n)
\end{Bmatrix},
\tag{30}
$$

where the submatrices of the new dynamic stiffness matrix $\hat{\tilde{\mathbf{K}}}$ are defined as

$$
\hat{\tilde{\mathbf{K}}}_{11} = \hat{\mathbf{K}}_{11}^{(1)} - \hat{\mathbf{K}}_{12}^{(1)}(\hat{\mathbf{K}}_{22}^{(1)} + \hat{\mathbf{K}}_{11}^{(2)})^{-1}\mathbf{X}_2,
\tag{31}
$$

$$
\hat{\tilde{\mathbf{K}}}_{12} = \hat{\mathbf{K}}_{12}^{(1)}(\hat{\mathbf{K}}_{22}^{(1)} + \hat{\mathbf{K}}_{11}^{(2)})^{-1}\hat{\mathbf{K}}_{12}^{(2)}\mathbf{X}_1^{-1}\hat{\mathbf{K}}_{12}^{(3)},
\tag{32}
$$

$$
\hat{\tilde{\mathbf{K}}}_{21} = \hat{\mathbf{K}}_{21}^{(3)}\mathbf{X}_1^{-1}\hat{\mathbf{K}}_{21}^{(2)}(\hat{\mathbf{K}}_{22}^{(1)} + \hat{\mathbf{K}}_{11}^{(2)})^{-1}\hat{\mathbf{K}}_{21}^{(1)},
\tag{33}
$$

$$
\hat{\tilde{\mathbf{K}}}_{22} = \hat{\mathbf{K}}_{22}^{(3)} - \hat{\mathbf{K}}_{21}^{(3)}\mathbf{X}_1^{-1}\hat{\mathbf{K}}_{12}^{(3)},
\tag{34}
$$

$$
\mathbf{X}_1 = (\hat{\mathbf{K}}_{22}^{(2)} + \hat{\mathbf{K}}_{11}^{(3)}) - \hat{\mathbf{K}}_{21}^{(2)}(\hat{\mathbf{K}}_{22}^{(1)} + \hat{\mathbf{K}}_{11}^{(2)})^{-1}\hat{\mathbf{K}}_{12}^{(2)},
\tag{35}
$$

$$
\mathbf{X}_2 = \hat{\mathbf{K}}_{21}^{(1)} + \hat{\mathbf{K}}_{12}^{(2)}\mathbf{X}_1^{-1}\hat{\mathbf{K}}_{21}^{(2)}(\hat{\mathbf{K}}_{22}^{(1)} + \hat{\mathbf{K}}_{11}^{(2)})^{-1}\hat{\mathbf{K}}_{21}^{(1)}.
\tag{36}
$$

Eq. (30) is the equilibrium equation for the spectral element with embedded degraded zone, where only the degrees of freedoms at the end nodes 1, 2 need to be used while forming the global system of a damaged structures in frequency domain.

8. Parametric representation of signals due to wave scattering from damage

Analysis of acoustic-ultrasonic signals helps in obtaining important physical information like dispersion as a function of geometry and material constants. It also helps in extracting information about the effect of small

cracks and damage on the propagating waves, especially when the damage sizes are small compared to the geometric scale of the structure itself, which cause dispersion and reflection of waves. In this section we carry out spectral and time–frequency analysis and investigate the effect of perturbation of damage parameters like material degradation factors and damage size on the model based estimate (damage index, DI).

The propagation of wave packet in a dispersive medium $k = k(\omega)$ is given by the Fourier integral

$$s(x,t) = \frac{1}{2\pi} \int_{-\infty}^{+\infty} S(\omega) e^{i(\omega t - kx)} \, d\omega, \tag{37}$$

where $S(\omega)$ is a complex spectral function of the input signal and k is the wavenumber. In practice $s(x,t)$ could be in the unit of electrical voltage and it can be easily correlated to the field variable $u(x,t)$ or their gradients in the near field. The signal after propagation over a distance $x = L$ is considered as the output signal $s_2(t)$ and it can be expressed as

$$s_2(t) = s(x,t)|_{x=L} = \frac{1}{2\pi} \int_{-\infty}^{+\infty} (S(\omega)H(\omega)) e^{i(\omega t - kL)} \, d\omega, \tag{38}$$

where $H(\omega)$ describes the propagation of the wave in the dispersive medium and is given by

$$H(\omega) = \frac{S_2(\omega)}{S_1(\omega)} = e^{-ikL}, \tag{39}$$

where $S_1(\omega)$ and $S_2(\omega)$ are the Fourier transforms of the input signal $s_1(t)$ and the output signal $s_2(t)$, respectively.

In what follows, we shall use a simple transmission line model for simulating dispersion and scattering of analytic signal $s(x,t)$. Consider a cantilever beam with length L, cross-sectional area A, and density ρ. The wavelength of the elastic wave is assumed to be greater than the thickness of the beam and therefore it can be approximated as a plane wave propagating with an acoustic impedance $Z_p = \rho v A$ where v is the velocity of the wave. Interaction between the waves with damage leads to reflection due to the change in the acoustic impedance (ignoring any mode conversion). The reflection coefficient $R(\omega)$ due to damage can conveniently be expressed as

$$R(\omega) = \frac{Z_d - Z_p}{Z_d + Z_p}, \tag{40}$$

where Z_d is the acoustic impedance of the damage. If the damage is due to material degradation over a small length (l) of the beam, then Z_d is obtained as

$$Z_d = Z_p \frac{\alpha Z_p + j Z_p \tan(kl)}{Z_p + j \alpha Z_p \tan(kl)}, \tag{41}$$

where α is the material damage coefficient [32]. The wavenumber k used in Eq. (41) represents the fundamental anti-symmetric Lamb wave mode or the flexural mode (A_0) propagating in the beam. The reflected signal containing such damage information is then given by

$$s_d(t) = \frac{1}{2\pi} \int_{-\infty}^{+\infty} R(\omega) S(\omega) e^{i\omega t - kx} \, d\omega. \tag{42}$$

Damage parameter estimation can now be carried out with the known input signal, the known dispersion relation for the undamaged system and the unknown damage parameters. However, there could be difference between the experimental and the simulated wave propagation results and it is due to the presence of noise, modelling errors and model discretisation errors. Next, we calculate the bounds of this difference/error based on the energy of the signal. We focus our attention to the reflected signal from the damage and the energy bounds in terms of the damage parameters. Let us assume that the damage parameters α and l are perturbed by small parameters ε_1 and ε_2, respectively. By varying ε_1 and ε_2, the energy of the reflected signal from the damage is calculated. The signal is then analysed using signal processing techniques like FT, WT and HT to compute the energy of the coefficients. Substituting Eq. (41) in Eq. (40), the reflected signal coefficient $R(\omega)$ is

obtained as

$$R(\omega) = H(\omega) = \frac{Z_d - Z_p}{Z_d + Z_p} = \frac{Z_p \dfrac{Z_d + \mathrm{i}Z_p \tan(kl)}{Z_p + \mathrm{i}Z_d \tan(kl)} - Z_p}{Z_p \dfrac{Z_d + \mathrm{i}Z_p \tan(kl)}{Z_p + \mathrm{i}Z_d \tan(kl)} + Z_p}. \tag{43}$$

By assuming that $Z_d = \alpha Z_p$, the above equation is simplified into the following:

$$\begin{aligned} R(\omega) &= \frac{\dfrac{\alpha + \mathrm{i} \tan(kl)}{1 + \mathrm{i}\alpha \tan(kl)} - 1}{\dfrac{\alpha + \mathrm{i} \tan(kl)}{1 + \mathrm{i}\alpha \tan(kl)} + 1} \\ &= \frac{(1 - \alpha)(-1 + \mathrm{i} \tan(kl))}{(1 + \alpha)(1 + \mathrm{i} \tan(kl))} \\ &= \frac{(1 - \alpha)(1 + \alpha)^{-1}}{4}[-1 - \mathrm{e}^{-\mathrm{i}2kl} + \mathrm{i}(1 - \mathrm{e}^{-\mathrm{i}2kl})]. \end{aligned} \tag{44}$$

By using the binomial series expansion in terms of α and exponential series expansion in terms of kl and neglecting the higher-order terms $O(\alpha^3)$, $O(kl^3)$, Eq. (44) is simplified to the following:

$$\begin{aligned} R(\omega) &\simeq \frac{1}{4}(1 - \alpha)(1 - \alpha + \alpha^2)(-1 - (1 + \mathrm{i}2kl - 2k^2l^2)) \\ &\quad + \mathrm{i}(1 - (1 - \mathrm{i}2kl + 2k^2l^2)) + O(\alpha^3) + O(k^3l^3) \\ &\simeq \frac{(1 - 2\alpha + 2\alpha^2)}{4}(-2 - \mathrm{i}2kl + 2k^2l^2 - 2kl - \mathrm{i}2k^2l^2) + O(\alpha^3) + O(k^3l^3). \end{aligned} \tag{45}$$

With perturbation $\alpha \leftarrow \alpha(1 + \varepsilon_1)$ and $l \leftarrow l(1 + \varepsilon_2)$, where ε_1 and ε_2 are two small parameters, Eq. (45) becomes

$$R(\omega, \varepsilon_1, \varepsilon_2) \simeq \tfrac{1}{4}[1 - 2\alpha(1 + \varepsilon_1) + 2\alpha^2(1 + \varepsilon_1)^2][-2 - 2kl(1 + \varepsilon_2)(1 + i) + 2k^2l^2(1 + \varepsilon_2)^2(1 - i)]. \tag{46}$$

By grouping the constant terms with ε_0, ε_1 and ε_2, one has

$$R(\omega) = \varepsilon_0 R_{\varepsilon_0} + \varepsilon_1 R_{\varepsilon_1} + \varepsilon_2 R_{\varepsilon_2}, \tag{47}$$

where

$$\begin{aligned} R_{\varepsilon_0}(\omega, \alpha, l, k) &= (\tfrac{1}{2} - \alpha + \alpha^2)(-1 + (-1 - i)kl + (1 - i)k^2l^2), \\ R_{\varepsilon_1}(\omega, \alpha, l, k) &= (-1 - i)(\tfrac{1}{2} - \alpha + \alpha^2)kl - \alpha(-1 + (-1 - i)kl + (1 - i)k^2l^2) + O(\varepsilon_1^2), \\ R_{\varepsilon_2}(\omega, \alpha, l, k) &= 2(-1 - i)\alpha^2 kl + (1 - i)(1 - 2\alpha + 2\alpha^2)k^2l^2 \\ &\quad + 2\alpha^2(-1 + (-1 - i)kl + 2(1 - i)k^2l^2) + O(\varepsilon_1\varepsilon_2) + O(\varepsilon_2^2). \end{aligned} \tag{48}$$

The reflected signal due to damage has now the form

$$\begin{aligned} S_d(\omega) &= R(\omega)S(\omega) \\ &= \varepsilon_0 R_{\varepsilon_0}(\omega)S(\omega) + \varepsilon_1 R_{\varepsilon_1}(\omega)S(\omega) + \varepsilon_2 R_{\varepsilon_2}(\omega)S(\omega). \end{aligned} \tag{49}$$

In mathematics, a Sobolev space is defined as the space of p-power integrable functions and the ultrasonic signals fall under the space of square integrable functions, that is, $p = 2$. The norm for L^2 space is given by

$$\|f\|^2 = \int_{-\infty}^{+\infty} |f|^2 \, \mathrm{d}t. \tag{50}$$

We now define spectral energy of S_d in Eq. (49) as $\|S_d(\omega)\|^2$. By applying the Cauchy–Schwarz inequality in Eq. (49), we get

$$
\begin{aligned}
\|S_d(\omega)\|^2 &= \|\varepsilon_0 R_{\varepsilon_0}(\omega)S(\omega) + \varepsilon_1 R_{\varepsilon_1}(\omega)S(\omega) + \varepsilon_2 R_{\varepsilon_2}(\omega)S(\omega)\|^2 \\
&\leqslant \varepsilon_0^2 \|R_{\varepsilon_0}(\omega)S(\omega)\|^2 + \varepsilon_1^2 \|R_{\varepsilon_1}(\omega)S(\omega)\|^2 + \varepsilon_2^2 \|R_{\varepsilon_2}(\omega)S(\omega)\|^2.
\end{aligned}
\tag{51}
$$

In order to see how different the simulated results are from the experimental results, we need a way to bound the differences between them. The spectral energy bounds from Eq. (51) provides an estimate of the variation in the spectral energy of the damage signal as a function of the damage length and the material degradation factor. Here we have divided the problem into two sub-problems, firstly the energy contribution from the ε_0 term representing the energy contribution of the smaller scales and secondly the energy contributions from the parameters $\varepsilon_1, \varepsilon_2$ which are the correction terms from the large scales to the small scales. In this formulation we have not taken into account the presence of noise in the signal. The energy contributions from the ε_0 term are obtained from simulation with known material and geometric parameters and this in general will either be a lower or upper bound to the experimental results. The energy contributions from the terms with $\varepsilon_1, \varepsilon_2$ provides an analytical estimate of the differences between the experimental and simulated results. This correction term helps in providing a bound from the signal processing point of view. The drawback in this method is that it does not provide any information regarding the way in which energy is varying with time and frequency of the signal. Therefore, we extend this study using WT and HHT.

First, we study the signal due to damage and apply WT. The transformed signal can be expressed as

$$
\hat{S}_d(b,a)_{\mathrm{WT}} = \frac{1}{\sqrt{a}} \int_{-\infty}^{+\infty} S_d(t)\psi^*\left(\frac{t-b}{a}\right) \mathrm{d}t.
\tag{52}
$$

The above equation in the frequency domain is expressed as

$$
\hat{\hat{S}}_d(b,a)_{\mathrm{WT}} = \sqrt{a} \int_{-\infty}^{+\infty} S_d(\omega)\hat{\psi}^*(a\omega)\mathrm{e}^{\mathrm{i}2\pi b\omega} \mathrm{d}\omega.
\tag{53}
$$

The energy of the wavelet coefficients is given by

$$
\begin{aligned}
\|\hat{\hat{S}}_d(b,a)_{\mathrm{WT}}\|^2 &= \left\| \sqrt{a} \int_{-\infty}^{+\infty} S_d(\omega)\hat{\psi}^*(a\omega)\mathrm{e}^{\mathrm{i}2\pi b\omega} \mathrm{d}\omega \right\|^2 \\
&= a\|S_d(\omega)\hat{\psi}^*(a\omega)\|^2.
\end{aligned}
\tag{54}
$$

The energy density of the wavelet coefficient is bounded as follows:

$$
\begin{aligned}
\|\hat{\hat{S}}_d(b,a)_{\mathrm{WT}}\|^2 &= a\|\{\varepsilon_0 R_{\varepsilon_0}(\omega)S(\omega) + \varepsilon_1 R_{\varepsilon_1}(\omega)S(\omega) + \varepsilon_2 R_{\varepsilon_2}(\omega)S(\omega)\}\hat{\psi}^*(a\omega)\|^2 \\
&\leqslant a\varepsilon_0^2 \|R_{\varepsilon_0}(\omega)\hat{\psi}^*(a\omega)S(\omega)\|^2 + a^2\varepsilon_1^2 \|R_{\varepsilon_1}(\omega)\hat{\psi}^*(a\omega)S(\omega)\|^2 \\
&\quad + a\varepsilon_2^2 \|R_{\varepsilon_2}(\omega)\hat{\psi}^*(a\omega)S(\omega)\|^2.
\end{aligned}
\tag{55}
$$

The energy distribution among $(\varepsilon_1, \varepsilon_2)$ terms provides additional information to the simulated signal and helps in accounting for the terms missing in the numerical model.

Next, let us consider the same signal due to damage by applying the HT. The IMFs obtained from EMD are studied using HT to extract the instantaneous frequency. The HT changes only the phase of the signal with effect on the signal amplitude. The main idea of applying HT here is to make the signal analytic resulting in only positive frequencies. The HT of the signal is given by

$$
v(t) = -\frac{1}{\pi}\mathrm{PV} \int_{-\infty}^{+\infty} \frac{u(\eta)}{\eta - t} \mathrm{d}\eta,
\tag{56}
$$

where PV is the principal value of the cauchy integral. One can simplify the integral and write

$$
v(t) = u(t) * \frac{1}{\pi t},
\tag{57}
$$

where $*$ describes the convolution operator. In the frequency domain, HT of $v(t)$ is expressed as

$$\hat{v}(\omega) = -i\,\text{sgn}(\omega)U(\omega). \tag{58}$$

Next, the HT is applied to the signal due to damage. This can be expressed as

$$q(t) = s_d(t) + i\,\text{HT}[s_d(t)],$$

$$\hat{Q}(\omega) = S_d(\omega) + i[-i\,\text{sgn}(\omega)S_d(\omega)]$$
$$= [1 + \text{sgn}(\omega)]S_d(\omega),$$

$$1 + \text{sgn}(\omega) = \begin{cases} 2 & \text{for } \omega > 0, \\ 1 & \text{for } \omega = 0, \\ 0 & \text{for } \omega < 0. \end{cases} \tag{59}$$

We find that the energy density of the HT is bounded in the following form:

$$\|\hat{Q}(\omega)\|^2 = [1 + \text{sgn}(\omega)]^2 \|\varepsilon_0 R_{\varepsilon_0}(\omega)S(\omega) + \varepsilon_1 R_{\varepsilon_1}(\omega)S(\omega) + \varepsilon_2 R_{\varepsilon_2}(\omega)S(\omega)\|^2$$
$$\leqslant [1 + \text{sgn}(\omega)]^2 \{\varepsilon_0^2 \|R_{\varepsilon_0}(\omega)S(\omega)\|^2 + \varepsilon_1^2 \|R_{\varepsilon_1}(\omega)S(\omega)\|^2 + \varepsilon_2^2 \|R_{\varepsilon_2}(\omega)S(\omega)\|^2\}. \tag{60}$$

8.1. Numerical example

A AS/3505-6 graphite-epoxy laminated composite cantilever beam of length 0.8 m and having a cross-sectional area 10 mm thickness $\times$ 10 mm width is considered in this example. Material degradation in the beam is modelled using spectral finite element method with the damage parameters $\alpha = 0.35$, $l = 0.03$ m. The damage is present at a distance of 0.4 m form the fixed end of the beam. A single frequency tone-burst sinusoidal pulse modulated at 20 kHz is applied transversely at the tip cross-section to generate the A_0 mode and the reflected signal is picked up at the same position. The effect of the small parameters $\varepsilon_1, \varepsilon_2$ on the energy density of FT, WT and HT techniques are studied as follows.

The spectral energy bounds of the reflected signal from the damage are calculated using Eq. (51). The effect of the small parameters $\varepsilon_1, \varepsilon_2$ are studied by varying them independently. First, ε_1 is varied and the spectral energy density is plotted as shown in Fig. 6(a). The effect of ε_1 is negligible on the spectral energy density. Next, ε_2 is varied and Fig. 6(b) shows the corresponding spectral energy density. Here the effect of ε_2 is more compared to ε_1 and it implies that a small perturbations of the length of the damage has more effect compared to the perturbation of the material degradation parameter on the power spectral density.

Next, we compute the wavelet spectral energy bounds of the damage signal in the time–frequency plane using Eq. (55). The wavelet energy density values are computed for the input signal frequency of 20 kHz and
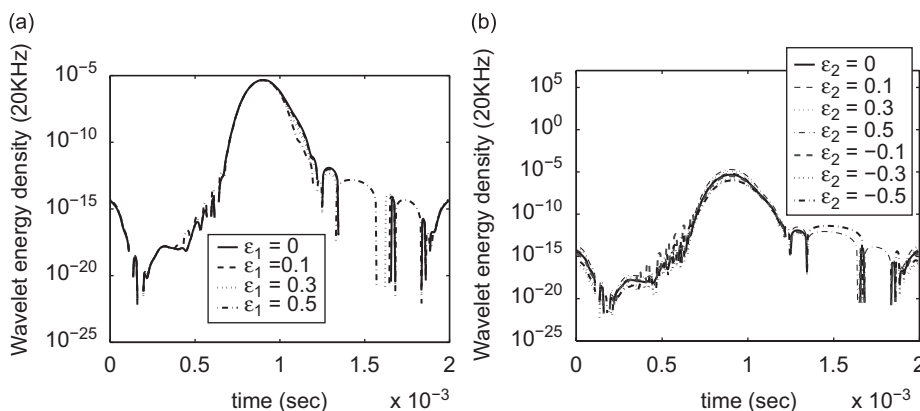

Fig. 7. Wavelet energy density for: (a) various ε_1, $\varepsilon_2 = 0$; (b) various ε_2, $\varepsilon_1 = 0$ (numerical example in Section 8.1).
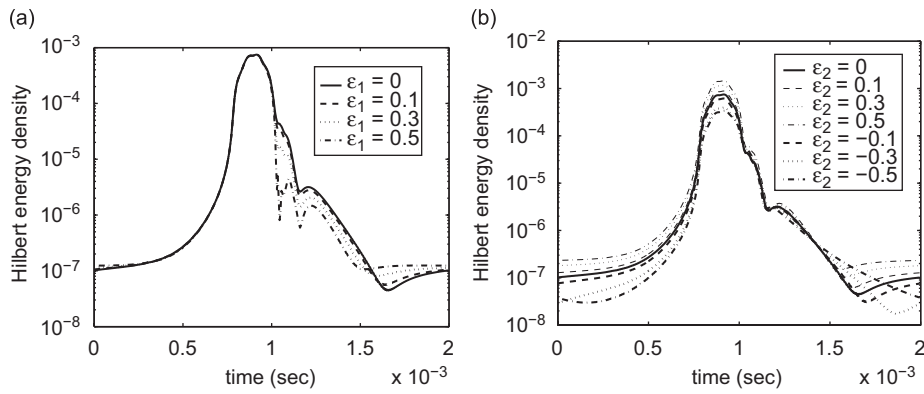
Fig. 8. Hilbert energy density for: (a) various ε_1, $\varepsilon_2 = 0$; (b) various ε_2, $\varepsilon_1 = 0$ (numerical example in Section 8.1).

the effect of $(\varepsilon_1, \varepsilon_2)$ on wavelet spectral energy density is shown in Fig. 7. As observed in the spectral domain, the effect of ε_2 is more compared to ε_1 on the wavelet spectral energy density. Similarly, we also compute the Hilbert energy bounds using Eq. (60) in the time–frequency plane. The Hilbert energy density is computed by varying $\varepsilon_1, \varepsilon_2$ and plotted in Fig. 8. The result shows that the effect of ε_1 is again less compared to ε_2 on the Hilbert energy density computed on reflected signal from damage.

9. Damage index

DI provides a measure of the damage in the structure by studying the signals scattered from the damage. DI measures based on signal processing have been reported by Jeong et al. [33]. In that study, DI was defined as the ratio of the scattered energy of the S_0 mode to the baseline energy of the S_0 mode. In the present approach, we define DI as the L^2 norm of the WT and HHT coefficients due to the reflected signal from the damage. Effect of structural boundary, etc. on the reflected signal is eliminated either using a baseline model or measurement on the healthy structure. We make use of the following definition of DI based on WT given by

$$\mathrm{DI_{WT}} = \sum_{i=1}^{N} \| \hat{x}(a,b)_{\mathrm{WT}_i} \|^2, \tag{61}$$

where N is the total number of sampling points on the time axis. In the case of HHT, DI is computed as the L^2 norm of the instantaneous amplitude of the signal and expressed as

$$\mathrm{DI_{HHT}} = \sum_{i=1}^{N} \| a(t_i) \|^2. \tag{62}$$

The DIs are proportional to the energy of the wave reflected from the damage and provides information about the size of the damage.

10. Analysis of experimental signals from a cracked beam

An experiment is conducted on an aluminum beam of length 0.5 m and thickness 4 mm. The main focus here is to detect damage, if any, from the experimental signals. Excitation signal is generated through two 1 mm thick PZT crystals, one bonded at the top surface and the other bonded at the bottom surface near the root of the beam as shown in Fig. 9. Single-axis accelerometers are placed at the baseline model nodes as shown in Fig. 10(a) for the eight-sensor configurations. The mid-span crack is throughwidth and is of 2 mm thickness and 0.75 mm slot-width. The two ($30 \times 30 \times 10\,\mathrm{mm}^3$) PZT crystals are excited in d_{31} mode (transversely polarised mode) of the beam using power amplifier, which is driven by DSPACE DS 2103 DAQ board. A pulse of 1 ms duration with peak voltage of 100 V and of similar shape shown in Fig. 10(b) is employed to

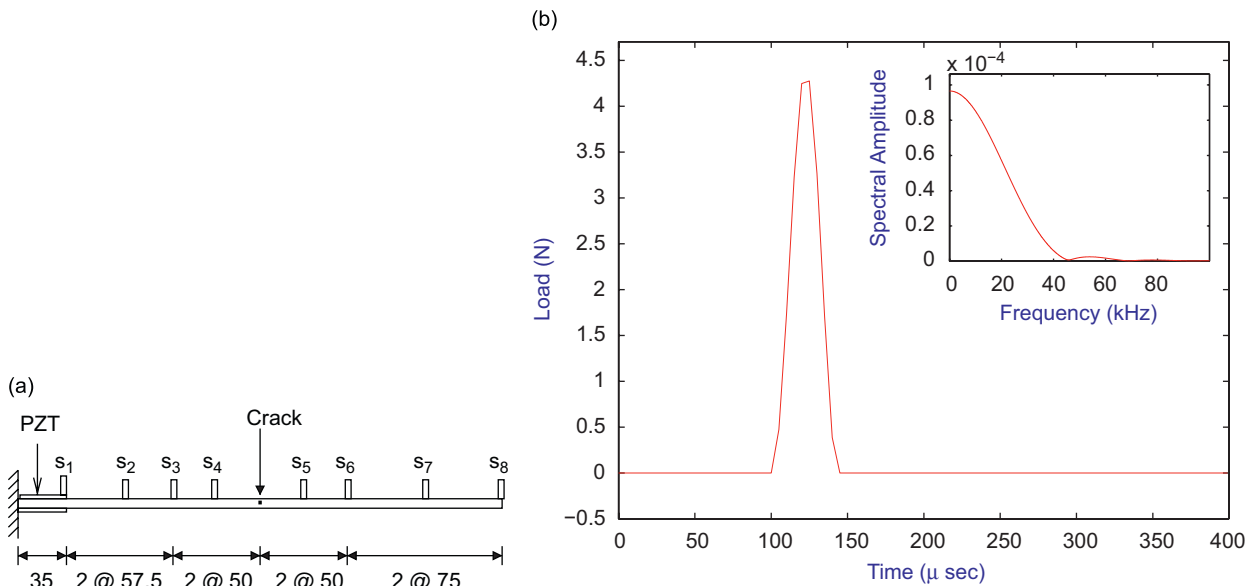Fig. 9. Instrumented sample with eight-sensor configuration.

Fig. 10. Aluminum cantilever beam with through-width 2 mm crack at the mid-span and PZT patches for diagnostic signal generation: (a) eight-sensors configuration with accelerometers; (b) a high frequency pulse used to study the response of the cracked composite beams. The spectral amplitude $\hat{f}$ over the frequency axis is shown in inset.

excite the PZT crystals connected in parallel. All other nodal forces are zero because no load is applied at these nodes. The sampling time for both the signal generation as well as acquisition is 27.26 μs. Figs. 9 and 10 show the instrumented samples with the PZT crystals, accelerometers and the slotted crack with 0.75 mm clearing. Figs. 11(a)–(e) and 12(a)–(e) show the acceleration histories at various loading states measured from the sensor s_4 on the left side of the crack, and also from sensor s_5 on the right side of the crack. It can be observed from Figs. 11 and 12 that the presence of crack causes deviation in the response in the sensors s_4 and s_5. WT is applied to the acceleration signals at various time instances of the progressive failure of the beam under tip loading for both the sensors s_4 and s_5. The WT coefficients $|\mathrm{WT}(a,b)|$ at frequency 1 kHz is computed and plotted at various time instants as shown in Fig. 13. The time stamp t_1 indicated no load and the time stamp t_6 indicates complete failure of the beam by plastic hinge formation at the crack location. The crack reflects the incident wave back to sensor s_4. As a result, the wavelet coefficient value increases as the crack grows. But the crack transmits less energy across it to the sensor s_5, which indicates decrease in the wavelet coefficients as
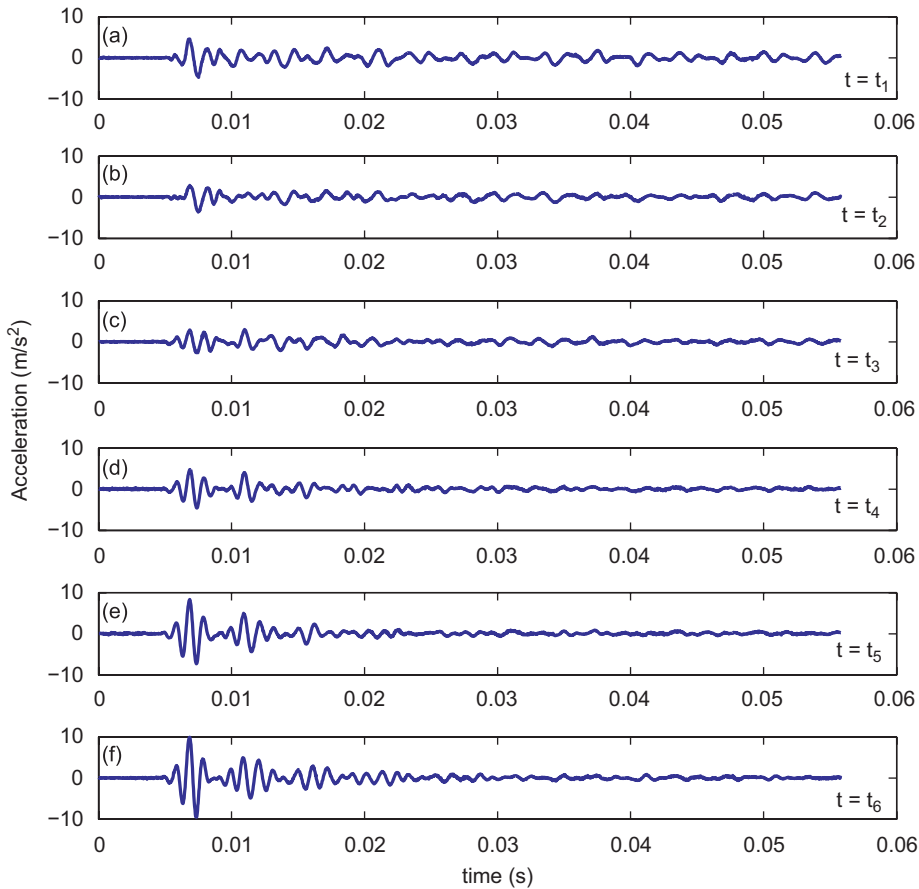
Fig. 11. Experimental signals measured from sensor 4 at various instants of time: (a) signal without loading at the tip; (b)–(e) signals during growth of crack; (f) signal for the case of crack grown up to 3 mm and complete failure of the beam under plastic hinge formation.

the beam tends to failure. The signal from sensors s_4 and s_5 are also studied using HHT technique. The unwrapped phase is computed at various loading instants and shown in Fig. 14. The presence of crack reflects the waves with higher amplitude at s_4 and leads to more oscillations. As a result, the unwrapped phase increases with the growing crack. Less energy is transferred across the crack to s_5, which leads to less oscillation in the signal and therefore it reduces the unwrapped phase at the subsequent load instants. Thus WT and HHT based approaches are able to distinguish the presence of progressive damage in the form of crack in a beam.

11. Numerical simulation of damage parameter sensitivities

11.1. Effect of delamination parameters

A AS/3505-6 graphite-epoxy laminated composite cantilever beam of length 800 mm and having a cross-sectional area 16 mm thickness ×10 mm width is considered for this study. Numerical simulation is performed using single spectral element with damage and with 4096 FFT sampling points ($\Delta\omega = 48.828$ Hz). A single frequency tone-burst sinusoidal pulse modulated at 20 kHz (Fig. 15) is applied transversely at the tip cross-section to generate the first antisymmetric mode (A_0) in the beam. Keeping the right tip of the delamination at a fixed distance $L_1 = 0.6$ m from node 2, delamination length L_2 is varied from 20 to 215 mm with an increment of 5 mm at every step. The transverse velocity at the tip is plotted in Fig. 16. Variation in the amplitude of the reflected wave from the delamination tip as function of the delamination length is found to be
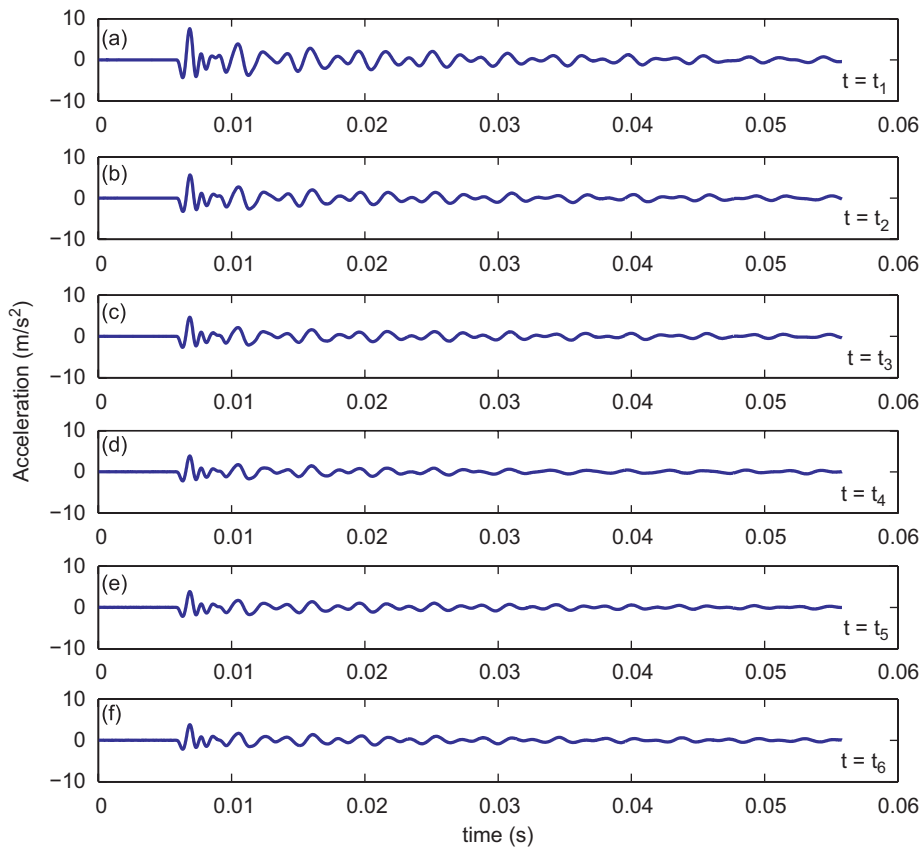
Fig. 12. Experimental signals measured from sensor 5 at various instants of time: (a) signal without loading at the tip; (b)–(e) signals during growth of crack; (f) signal for the case of crack grown up to 3 mm and complete failure of the beam under plastic hinge formation.
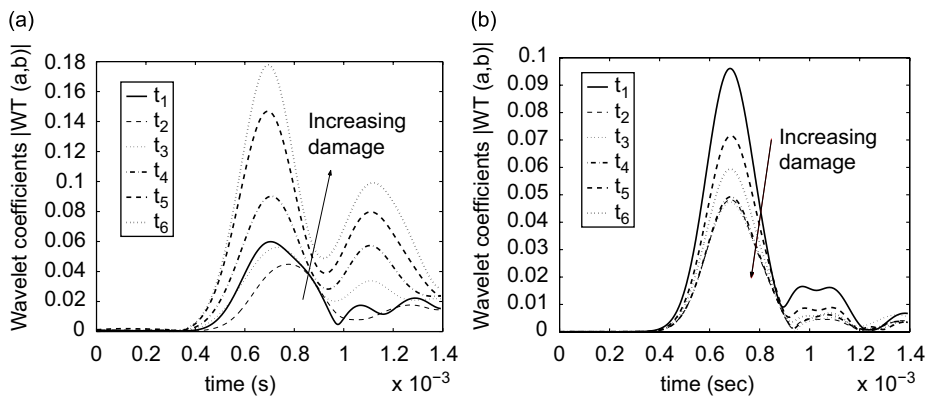

Fig. 13. Wavelet coefficient at various time instants of progressive failure of the cracked beam: (a) signal from sensor 4 (see Fig. 11); (b) signal from sensor 5 (see Fig. 12).

periodic in nature. It is diminishing near those values of the delamination lengths which are in integer multiple of half of the group wavelength λ_g. The group speed is calculated as $c_g = 2724\,\text{m/s}$. Now, considering the frequency of excitation $\omega = 20\,\text{kHz}$, we compute the group wavelength as $\lambda_g = c_g/\omega \approx 136\,\text{mm}$. The reason for this periodicity of $\lambda_g/2$ can be attributed to the cancellation or amplification of the scattered waves from the two tips of the delamination. For those lengths of the delamination, which are near integer multiple of $\lambda_g/2$, the reflection generated by one tip of delamination is attenuated by the reflection generated by the other
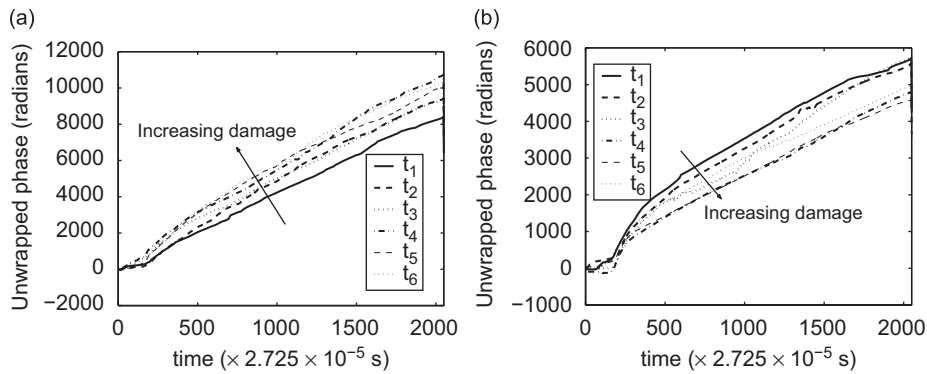
Fig. 14. (a) Hilbert Huang transform—unwrapped phase at various time instants of progressive failure of the cracked beam: (a) signal from sensor 4 (see Fig. 11); (b) signal from sensor 5 (see Fig. 12).
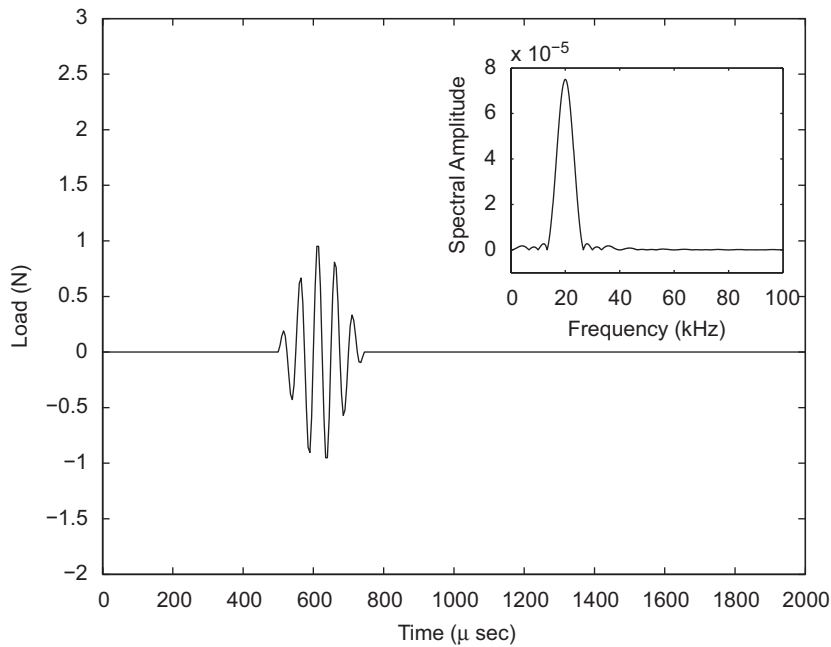
Fig. 15. Single frequency tone-burst sinusoidal pulse modulated at 20 kHz using trapezoidal window. The spectral amplitude $\hat{f}$ over the frequency axis is shown in inset.

tip being out of phase. Complete cancellation of the reflection is not possible because of some dispersiveness of the scattered wave. WT is applied to study the signals reflected from the delamination of various lengths. The wavelet coefficients are shown in Fig. 17. From Fig. 17, it is clear that the value of wavelet coefficients are small for lengths of delamination which are near integer multiple of $\lambda_g/2$. Similar behaviour is seen in the variation of magnitude of HHT as shown in Fig. 18. The DI for delamination using WT is calculated by taking the square norm of the wavelet coefficients at the input signal frequency of 20 kHz. For HHT, the DI is computed by taking the square of the norm of the instantaneous amplitude of the first IMF of the signal. The DI computed for various delamination lengths using WT and HHT are shown in Fig. 19. It is clear from the figure that the value of DI is very small when the delamination length is of the order of $\lambda_g/2$.
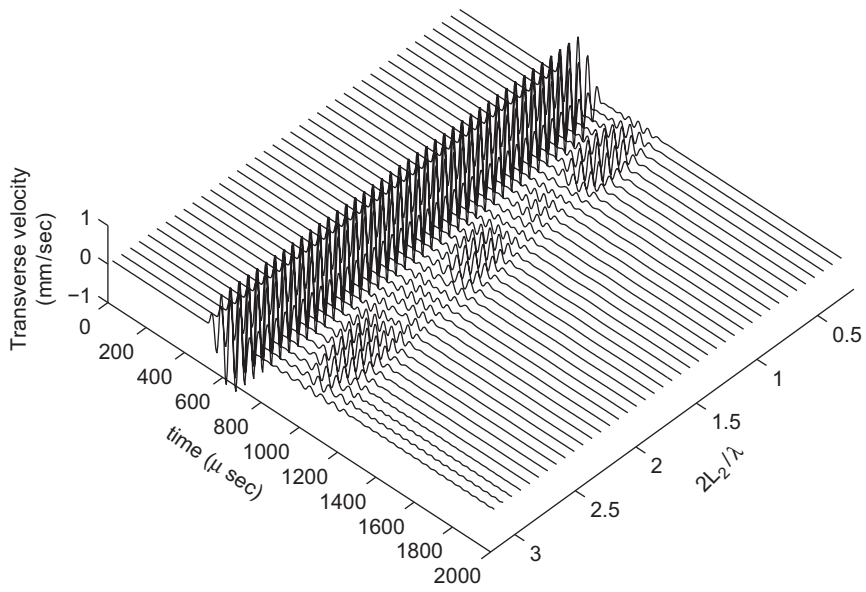
Fig. 16. Transverse velocity history computed at node-2 for different lengths (L_2) of delamination [5].
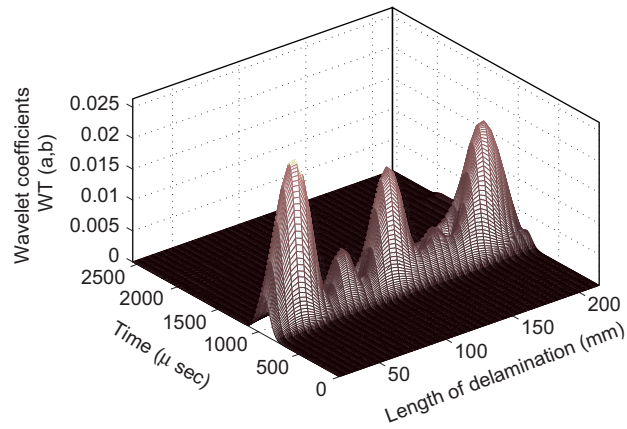

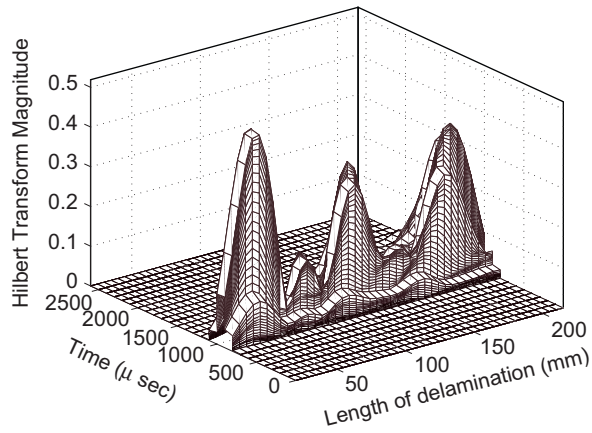Fig. 17. Wavelet coefficients for delamination of various lengths using narrow-band signals.

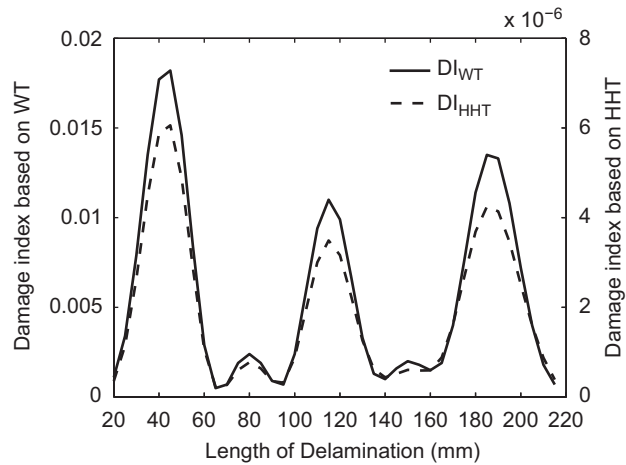Fig. 18. Hilbert transform magnitude for delamination of various lengths using narrow-band signals.

Fig. 19. Damage index based on WT and HHT for delamination of various lengths.
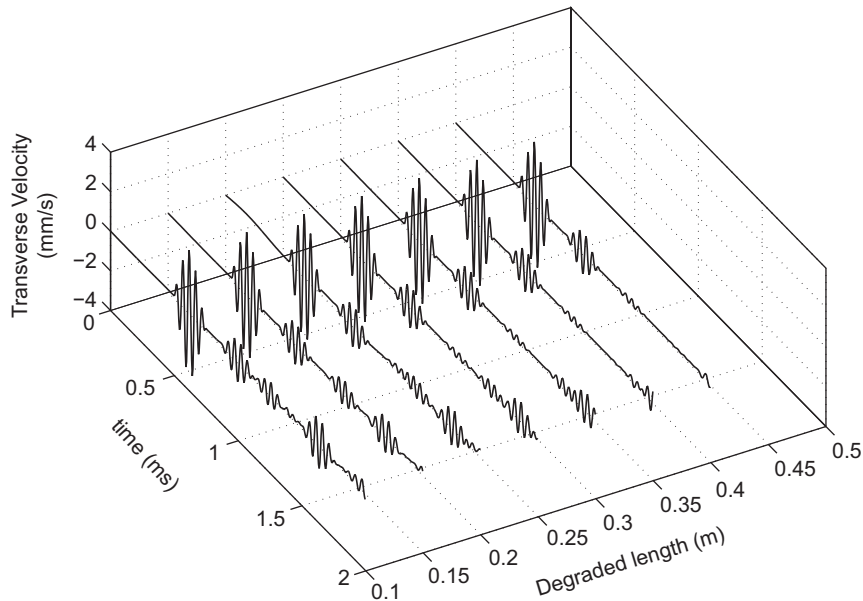

Fig. 20. Transverse velocity histories due to variation in the length of the degraded zone under narrow-band diagnostic signal (see Fig. 5). Degradation factor $\alpha_{11} = 0.2$.

11.2. Material degradation due to transverse matrix crack in composite

In order to simulate the effect of stiffness degradation on the diagnostic signal, a AS/3505-6 graphite-epoxy laminated composite cantilever beam of length 800 mm, thickness 16 mm and width 10 mm is considered. All the plies are assumed to be of equal thickness with stacking sequence $(0^\circ_{40}/90^\circ_{80}/0^\circ_{40})$, here the subscript indicates the number of plies. It is assumed that all the 90° plies are degraded with same factor of α_{11} (Eq. (25)). The dynamic force as considered earlier in Fig. 15 is applied in the transverse direction at the tip to generate the A_0 mode in the beam. We assumed that the plies were degraded uniformly within the degraded zone.
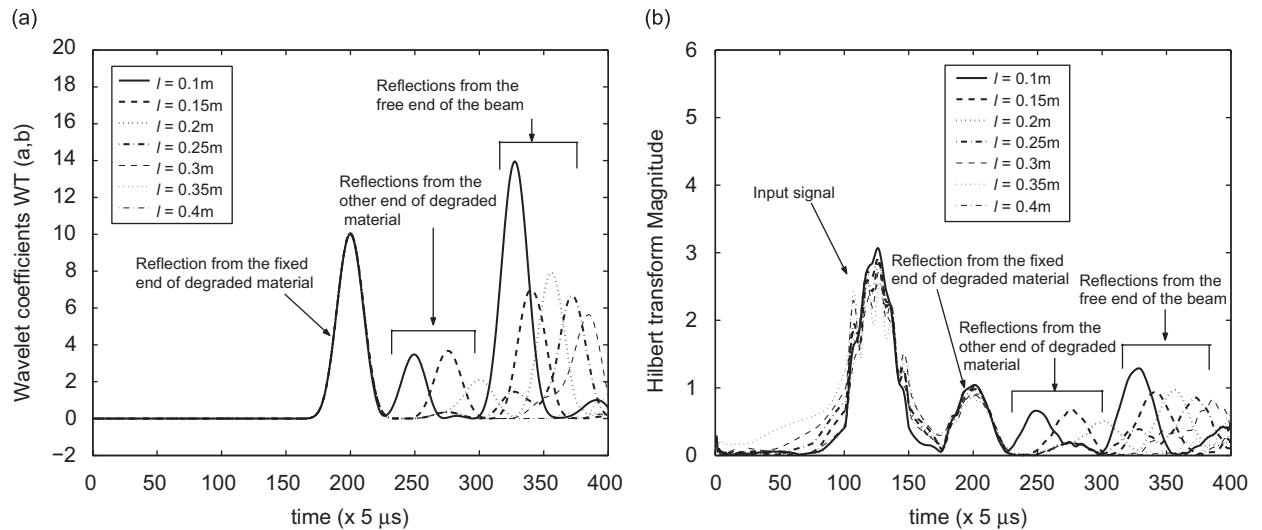
Fig. 21. (a) Wavelet coefficients; (b) Hilbert transform magnitude coefficients, for material degradation of various lengths (l) when subjected to band loading (see Fig. 20).

In order to study the effect of the length of the degraded zone, we consider the same cantilever beam as considered above with one of the interface fixed at 0.4 m distance from the tip. The length of the degraded zone is varied by moving the other interface towards the fixed-end from 0.1 to 0.4 m. The last case represents one half of the beam on the fixed-end side of the beam as degraded. The transverse velocity histories at the tip of the beam for this variation in the size of degraded zone are shown in Fig. 20 for $\alpha_{11} = 0.2$. From Fig. 20, it can be seen that for smaller size of the degraded zone with degradation ($\alpha_{11} = 0.2$), both the reflections from the two interfaces are easily detectable. WT and HHT are applied to the simulated signals of material degradation of various lengths. In the case of WT, the wavelet coefficients at 20 kHz, and for HHT the instantaneous amplitude of the signal are shown in Fig. 21 for various length of degraded zone. The reflections from the damage and free-end of the beam are clearly seen. The amplitude of the reflections seems to decrease with the increase in the degradation length as the energy is absorbed across the damage.

Next, we consider a broad-band Gaussian type pulse to study the response of the degraded zone. This constitutes a truly multiresolution problem. Fig. 10(b) shows the time history of a Gaussian pulse having a frequency content up to 40 kHz (shown in the figure inset). Here it is important to note that in order to interrogate using a particular wave mode, which is preferably less dispersive and produces a wavelength smaller than the damage size, the operating frequency of the transducers needs to be chosen optimally. At lower frequencies and for thinner structures, the dominant propagating wave modes are due to longitudinal elastic moduli. On the other hand, at higher frequencies and especially for a thicker structure, the dominant propagating modes are due to shear modulus and Poisson's ratio. Therefore, the damage models that should be used for numerical simulations and correlations between signal and damage parameters via experiments must include such frequency dependent factors adequately. In the present case, the chosen broad-band signal is such that it generate the A_0 mode in the beam and it is well below the cut-off frequency of all other higher-order Lamb wave modes. Hence the assumption of the degraded longitudinal modulus, undamaged transverse and shear moduli of the cross-ply, as in the earlier examples and also considered here, remains within the validity of the multiresolution analysis using WT and HHT.

In order to study the effect of the length of the degraded zone under the Gaussian pulse type excitation signal, we consider the same beam configuration as used for narrow-band pulse. The transverse velocity histories at the tip of the beam for variation in the size of degraded zone are shown in Fig. 22 for $\alpha_{11} = 0.2$. Processing of broad-band signal is more tedious compared to narrow-band signals and the dispersive nature of the waves in the composite beam makes the task more complicated. To simplify the problem, the wavelet coefficients at all the frequencies are summed together at each time instant for signals of different degradation
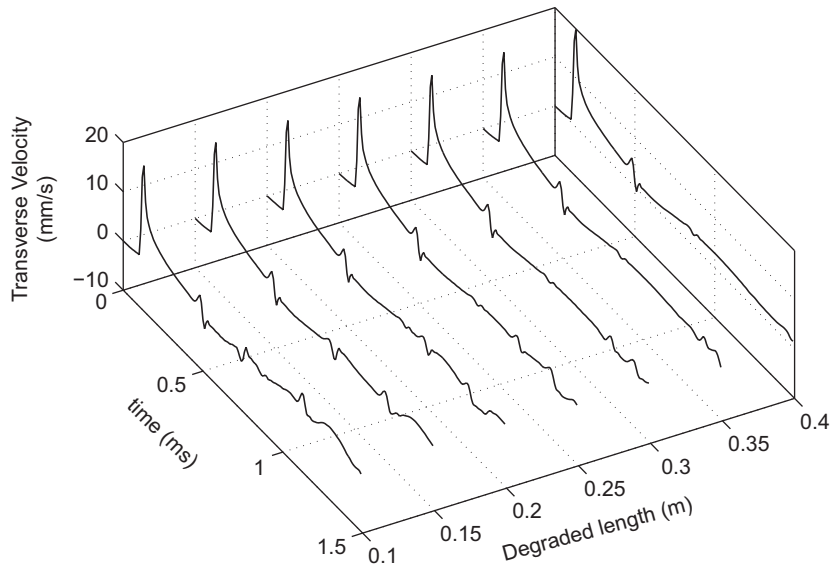
Fig. 22. Transverse velocity histories due to variation in the length of the degraded zone under pulse loading (see Fig. 5). Degradation factor $\alpha_{11} = 0.2$.
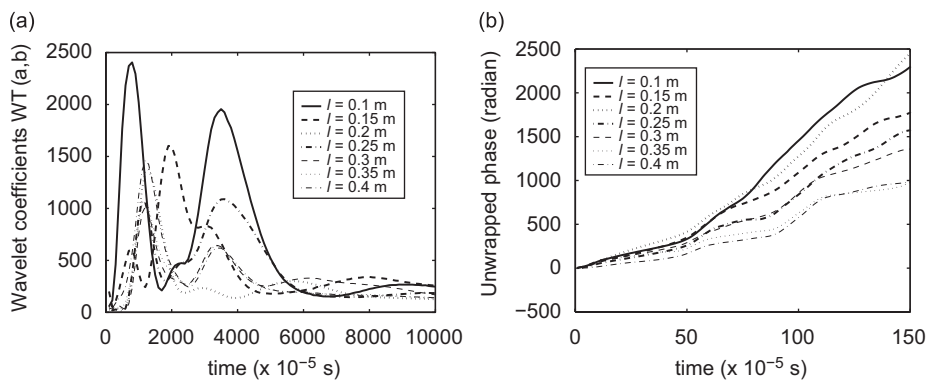

Fig. 23. (a) Wavelet coefficients; (b) Hilbert Huang transform—unwrapped phase, for material degradation of various lengths (l) under pulse loading (see Fig. 22).

lengths and they are shown in Fig. 23(a). The first set of peaks in the figure indicates the reflection from the fixed end of the damage and the second set of peaks represents the reflection from the varying end of the damage. Fig. 23(a) also shows clearly that the amplitude of the second reflection decreases with the increase in the damage size. In the case of HHT, the unwrapped phase of the signal of different degradation lengths are shown in Fig. 23(b). The variation of the unwrapped phase decreases with the damage length. This clearly indicates that the wave is absorbed and attenuated more as the length of degradation increases.

12. Conclusion

Time–frequency representations like wavelet transform (WT) and Hilbert–Huang transform (HHT) are employed to analyze the scattered wave signal due to damage from both experiments and simulations in order to identify the damage location and the dispersion of signal after they interact with various types of damages. Spectral finite elements are used to simulate the wave propagation in composites with delaminations and material degradation of various damage size. Both the narrow- and broad-band signals are employed to

interrogate the damages. In the case of narrow-band signals, WT and HHT are able to locate the damage and characterise its size. But for broad-band signals WT and HHT are able to only indicate the presence of damage and other informations are difficult to process, which is due to the dispersive nature of the broad-band signal. A damage index based on WT and HHT coefficients is proposed. For delamination lengths of the order of the wavelength of the incident wave, there is no reflection of wave from the damage and this result provides an insight of the interaction of the waves with damage. An analytical study is carried out to study the effects of higher-order scale damage parameters on the reflected wave signal. The reflected signal energy is found to be perturbed by higher-order scale parameters and their effect are studied in the spectral domain and also in the time–frequency domain. We are able to obtain the energy bounds analytically using FT, WT, HHT and this provides a good estimate of the error in the modelling of the wave propagation in a damaged structure. Sensitivity analysis based on TFR is performed. The results show variation of damage index with respect to the damage parameters like damage length and material degradation. Thus, the sensitivity analysis based on TFR helps in deducing important informations about the damage in the structure and ultimately helps in designing a reliable Structural Health Monitoring system.

References

[1] S. Gopalakrishnan, A. Chakraborty, D.R. Mahapatra, *Spectral Finite Element Method: Wave Propagation, Diagnostics and Control in Anisotropic and Inhomogeneous Structures*, Springer, Berlin, 2007.
[2] D.R. Mahapatra, S. Gopalakrishnan, T.S. Sankar, Spectral-element-based solution for wave propagation analysis of multiply connected composite beams, *Journal of Sound and Vibration* 237 (5) (2001) 819–836.
[3] D.R. Mahapatra, Development of Spectral Finite Element Models for Wave Propagation Studies, Health Monitoring and Active Control of Waves in Laminated Composite Structures, PhD Thesis, Indian Institute of Science, 2003.
[4] A.K. Garg, D.R. Mahapatra, S. Suresh, S. Gopalakrishnan, S.N. Omkar, Estimation of composite model damage parameters using spectral finite element and neural network, *Composite Science and Technology* 64 (2004) 2477–2493.
[5] A. Nag, D.R. Mahapatra, S. Gopalakrishnan, T.S. Sankar, A spectral finite element with embedded delamination for modeling of wave scattering in composite beams, *Composite Science and Technology* 63 (2003) 2187–2200.
[6] W. Ostachowicz, M. Krawczuk, M. Cartmell, M. Gilchrist, Wave propagation in delaminated beam, *Computers and Structures* 82 (2004) 475–483.
[7] M. Krawczuk, W. Ostachowicz, A. Zak, Modal analysis of cracked unidirectional composite beam, *Composites Part B: Engineering* 288 (1997) 641–650.
[8] W.M. Ostachowicz, Damage detection of structures using spectral finite element method, *Computers and Structures* 86 (2008) 454–462.
[9] S.T. Quek, Q. Wang, L. Zhang, K.H. Ong, Practical issues in detection of damage in beams using wavelets, *Smart Materials and Structures* 10 (2001) 1–9.
[10] S.T. Quek, P.S. Tua, Q. Wang, Detecting anomalies in beams and plate based on the Hilbert Huang transform of real signals, *Smart Materials and Structures* 12 (2003) 447–460.
[11] L. Cohen, *Time–frequency Analysis*, Prentice-Hall, Englewood Cliffs, NJ, 1995.
[12] S. Mallat, *A Wavelet Tour of Signal Processing*, Academic Press, New York, 1999.
[13] I. Daubechies, *Ten Lecture on Wavelets*, SIAM Publications, 1992.
[14] N.E. Huang, Z. Shen, S.R. Long, M.C. Wu, H.H. Shih, Q. Zheng, N.C. Yen, C.C. Tung, H.H. Liu, The empirical mode decomposition and the Hilbert spectrum for non-linear and non-stationary time series analysis, *Proceedings of the Royal Society of London Series A—Mathematical Physical and Engineering Sciences* 454 (1998) 903–995.
[15] H. Jeong, Y.-S. Jang, Wavelet analysis of plate wave propagation in composite laminates, *Composite Structures* 49 (2000) 443–450.
[16] W.H. Prosser, M.D. Seale, Time–frequency analysis of the dispersion of Lamb modes, *Journal of Acoustical Society of America* 105 (5) (1999) 2669–2676.
[17] C.A. Paget, S. Grondel, K. Levin, C. Delabarre, Damage assessment in composites by Lamb waves and wavelet coefficients, *Smart Materials and Structures* 12 (2003) 393–402.
[18] K.H. Ip, P.W. Tse, H.Y. Tam, Extraction of patch-induced Lamb waves using a wavelet transform, *Smart Materials and Structures* 13 (2004) 861–872.
[19] D. Pines, L. Salvino, Structural health monitoring using empirical mode decomposition and the Hilbert phase, *Journal of Sound and Vibration* 294 (2006) 97–124.
[20] H.G. Chen, Y.J. Yan, J.S. Jiang, Vibration based damage-detection in composite wingbox structures by HHT, *Mechanical Systems and Signal Processing* 21 (2007) 307–321.
[21] A. Apostoloudia, E. Douka, L.J. Hadjileontiadis, I.T. Rekanos, A. Trochidis, Time–frequency analysis of transient dispersive waves: a comparative study, *Applied Acoustics* 68 (2007) 296–309.
[22] S. Kadambe, G.F. Boudreaux-Bartels, A Comparison of the existence of crossterms in the Wigner distribution and the squared magnitude of the wavelet transform and the short time Fourier transform, *IEEE Transactions on Signal Processing* 40 (10) (1992) 2498–2516.

[23] R.T. Rato, M.D. Ortigueira, A.G. Batista, One the HHT, its problems, and some solutions, *Mechanical Systems and Signal Processing* 22 (6) (2008) 1374–1394.

[24] J.F. Doyle, *Wave Propagation in Structures*, Springer, Berlin, 1997.

[25] A.T. Patera, A spectral element method for fluid dynamics: laminar flow in a channel expansion, *Journal of Computational Physics* 54 (1984) 468–488.

[26] R. Sridhar, A. Chakraborty, S. Gopalakrishnan, Wave propagation analysis in anisotropic and inhomogeneous uncracked and cracked structures using pseudospectral finite element method, *International Journal of Solids and Structures* 43 (2006) 4997–5031.

[27] P. Kudela, M. Krawczuk, W. Ostachowicz, Wave propagation modelling in 1D structures using spectral finite elements, *Journal of Sound and Vibration* 300 (2007) 88–100.

[28] D.R. Mahapatra, S. Gopalakrishnan, T.S. Sankar, Scattering and transmission of mixed-mode waves in delaminated thick composite beams, *Proceedings of 2001 ASME Design Engineering and Technical Conference*, September 9–12, 2001, Pittsburgh, PA, USA, DETC01-VIB-21543.

[29] D.R. Mahapatra, D.R.S. Gopalakrishnan, A spectral finite element model for analysis of axial-flexural-shear coupled wave propagation in laminated composite beams, *Composite Structures* 59 (1) (2002) 67–88.

[30] W.M. Karunasena, A.H. Saha, S.K. Datta, Plane-strain wave scattering by cracks in laminated composite plates, *ASCE Journal of Engineering Mechanics* 117 (8) (1991) 1738–1754.

[31] N. Hu, H.H. Wang, B. Yan, H. Fukunaga, D.R. Mahapatra, S. Gopalakrishnan, The partition of unity finite element method for elastic wave propagation in Reissner–Mindlin plates, *International Journal of Numerical Methods in Engineering* 70 (2007) 1451–1479.

[32] M.-S. Choi, S.-Y. Kim, H. Kwun, G.M. Light, Transmission line model for simulation of guided-wave defect signals in piping, *IEEE Transactions on Ultrasonics, Ferroelectrics, and Frequency Control* 51 (2004) 640–643.

[33] J.-B. Ihn, F.K. Chang, Detection and monitoring of hidden fatigue crack growth using a built-in piezoelectric sensor/actuator network: I. Diagnostics, *Smart Materials and Structures* 13 (2004) 609–620.